Higgs boson production in e and real γ collisions

Norihisa Watanabe[*] and Yoshimasa Kurihara[†]

High Energy Accelerator Research Organization (KEK) Tsukuba, Ibaraki 305-0801, Japan

Tsuneo Uematsu[‡]

Institute for Liberal Arts and Sciences, Kyoto University, Kyoto 606-8501, Japan
and Maskawa Institute, Kyoto Sangyo University, Kyoto 603-8555, Japan

Ken Sasaki[§]

Dept. of Physics, Faculty of Engineering, Yokohama National University, Yokohama 240-8501, Japan

We investigate the Standard Model Higgs boson production in $e^-\gamma$ collisions. The electroweak one-loop contributions to the scattering amplitude for $e^-\gamma \to e^-H$ are calculated and expressed in analytical form. We analyze the cross section for the Higgs boson production in $e^-\gamma$ collisions for each combination of polarizations of the initial electron and photon beams. The feasibility of observing the Higgs boson in the $e^- + \gamma \to e^- + b + \bar{b}$ channel is examined.

PACS numbers: 12.15.-y, 13.66.Fg, 13.88.+e, 14.80.Bn

I. INTRODUCTION

A Higgs boson with mass about 125 GeV was discovered by ATLAS and CMS at LHC [1] and its spin, parity, and couplings to other particles have been examined [2]. For further detailed studies of its properties, a new accelerator facility, a linear e^+e^- collider, which offers much cleaner experimental collisions, is attracting growing attention [3]. Along with an e^+e^- collider, other options such as e^-e^-, $e^-\gamma$ and $\gamma\gamma$ colliders have also been discussed. See Refs. [4–8] and the references therein. Each option for colliders will provide interesting topics to study, such as the detailed measurement of the Higgs boson properties and the quest for the new physics beyond the Standard Model (SM). An e^-e^- collider is easier to build than an e^+e^- collider and may stand as a potential candidate before positron sources with high intensity are available. The $e^-\gamma$ and $\gamma\gamma$ options are based on e^-e^- collisions, where one or two of the electron beams are converted to the photon beams.

In this paper we investigate the production of the SM Higgs boson (H) in an $e^-\gamma$ collider.[1] We examine the reaction $e^-\gamma \to e^-H$ at the one-loop level in the electroweak interaction. Particularly, we are interested in the contribution from the two-photon fusion process $\gamma^*\gamma \to H$ which is described by the so-called transition form factor of the Higgs boson [9]. One of the advantages of linear colliders is that large polarization can be obtained for both beams. We analyze the Higgs boson production

cross section in $e^-\gamma$ collisions for each combination of polarizations of the initial electron and photon beams and discuss the feasibility of observing the Higgs bosons.

In fact, the Higgs boson production in $e^-\gamma$ collisions was investigated by Gabrielli, Ilyin and Mele some time ago before the Higgs boson was discovered [10] (see also Ref. [11]). They surveyed the reaction $e^-\gamma \to e^-H$ in the center-of-mass energy range $\sqrt{s} = (0.5–2)$ TeV and $m_h = (80–700)$ GeV. Comparing their results (at $\sqrt{s} = 500$ GeV and $m_h = 120$ GeV) with ours (at $\sqrt{s} = 500$ GeV and $m_h = 125$ GeV), we found some differences between the two. At the one-loop level in the electroweak interaction, four groups of Feynman diagrams, "$\gamma^*\gamma$," "$Z^*\gamma$," "$W\nu_e$," and "Ze" (which are defined in Sec. II), contribute to the reaction $e^-\gamma \to e^-H$. Although their result on the "$\gamma^*\gamma$" contribution is consistent with ours, the contributions from "$Z^*\gamma$" and "$W\nu_e$" were predicted to be much less than ours. Indeed, it was reported in Ref. [10] that the "$\gamma^*\gamma$" contribution was dominant in the total cross section and thus the interference effect among different groups of diagrams was rather small. We find that the "$Z^*\gamma$" contribution becomes approximately of the same magnitude as the one from "$\gamma^*\gamma$" at $\sqrt{s} = 500$ GeV. Also, for the case when the initial electron beam is left-handed, the "$W\nu_e$" contribution prevails over the "$\gamma^*\gamma$" at $\sqrt{s} = 500$ GeV. We will show that the interferences between "$\gamma^*\gamma$" and "$Z^*\gamma$" and between "$\gamma^*\gamma$" and "$W\nu_e$," which work destructively or constructively depending on the polarizations of the initial beams, are important factors affecting the behaviors of both the differential cross section and the cross section of the Higgs production. To make differences clear, we give explicit expressions for the results of our calculations.

---
[*]norihisa@post.kek.jp
[†]yoshimasa.kurihara@kek.jp
[‡]uematsu@scphys.kyoto-u.ac.jp
[§]sasaki@ynu.ac.jp
[1]A part of this work has been reported elsewhere [9].

In the next section, we classify the one-loop diagrams for the reaction $e^-\gamma \rightarrow e^- H$ into four groups. The contribution to the scattering amplitude from each group of the diagrams is evaluated in unitary gauge and expressed in analytical form. In Sec. III, the dependence of the reaction on the polarizations of the initial electron and photon beams is emphasized. Both the differential cross section and the cross section for $e^-\gamma \rightarrow e^- H$ are examined in each case of polarizations of the initial beams. In Sec. IV we consider the case when a high-intensity photon beam is produced by laser light backward scattering off a high-energy electron beam and we analyze the Higgs boson production in $e^-\gamma$ collisions using an e^-e^- collider machine. The final section is devoted to the conclusions. For completeness we add three Appendices where the Feynman rules we use are enumerated in Appendix A, the analytical expressions of the relevant scalar one-loop integrals are given in Appendix B and the contributions from the interference terms are written down in Appendix C.

II. HIGGS BOSON PRODUCTION IN $e^-\gamma$ COLLISIONS

We analyze the Higgs production in a e^- and real γ collision experiment,

$$e^-(k_1) + \gamma(k_2) \rightarrow e^-(k_1') + H(p_h). \quad (2.1)$$

The Higgs boson we consider is the one in the SM. The relevant Feynman diagrams for this process start not at tree level but at the one-loop level in the electroweak interaction. We calculate the relevant one-loop diagrams in unitary gauge using dimensional regularization which respects electromagnetic gauge invariance. In the unitary gauge, only the physical particles appear and ghosts and Goldstone bosons are absent. The gauge boson propagators in unitary gauge and the relevant Feynman rules for the three- and four-point
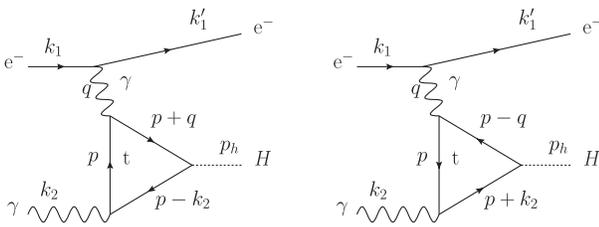

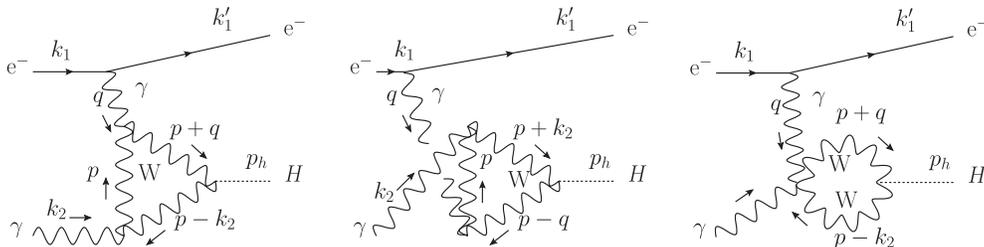FIG. 1. $\gamma^*\gamma$ fusion diagrams: top-quark loop contributions.

vertices which we use for this work are summarized in Appendix A. The one-loop diagrams which contribute to the reaction (2.1) are classified into four groups: $\gamma^*\gamma$ fusion diagrams (Figs. 1 and 2), $Z^*\gamma$ fusion diagrams, "$W\nu_e$" diagrams (Fig. 3) and "Ze" diagrams (Fig. 4).

Since k_2 is the momentum of a real photon, we have $k_2^2 = 0$ and $k_2^\beta \epsilon_\beta(k_2) = 0$, where $\epsilon_\beta(k_2)$ is the photon polarization vector. We set $q = k_1 - k_1'$. Assuming that electrons are massless so that $k_1^2 = k_1'^2 = 0$, we introduce the following Mandelstam variables:

$$s = (k_1 + k_2)^2 = 2k_1 \cdot k_2,$$
$$t = (k_1 - k_1')^2 = q^2 = -2k_1 \cdot k_1', \quad (2.2)$$

$$u = (k_1 - p_h)^2 = -2k_1' \cdot k_2 = m_h^2 - s - t, \quad (2.3)$$

where $p_h^2 = m_h^2$ with m_h being the Higgs boson mass.

A. Virtual photon-real photon fusion diagrams

Charged fermions and the W boson contribute to the one-loop $\gamma^*\gamma$ fusion diagrams. Note that one of the two γ's is virtual. Since the couplings of the Higgs boson to fermions are proportional to the fermion masses, we only consider the top quark for the charged fermion loop diagrams. The $\gamma^*\gamma$ fusion diagrams we calculate are shown in Figs. 1 and 2. The calculation is straightforward and we make full use of FEYNCALC [12]. We obtain the contribution from the one-loop $\gamma^*\gamma$ fusion diagrams to the gauge-invariant scattering amplitude as follows:

$$A_{\gamma\gamma} = \left(\frac{e^3 g}{16\pi^2}\right)[\bar{u}(k_1')\gamma_\mu u(k_1)]\frac{1}{t}\left(g^{\mu\beta} - \frac{2k_2^\mu q^\beta}{m_h^2 - t}\right)\epsilon_\beta(k_2)F_{\gamma\gamma},$$
$$(2.4)$$

with

$$F_{\gamma\gamma} = \frac{2m_t^2}{m_W}N_c Q_t^2 S_{(T)}^{\gamma\gamma}(t, m_t^2, m_h^2) - m_W S_{(W)}^{\gamma\gamma}(t, m_W^2, m_h^2),$$
$$(2.5)$$

where e and g are the electromagnetic and weak gauge couplings, respectively, and $N_c = 3$ and $Q_t = \frac{2}{3}$. $S_{(T)}^{\gamma\gamma}$ and

FIG. 2. $\gamma^*\gamma$ fusion diagrams: W-boson loop contributions.

$S^{\gamma\gamma}_{(W)}$ are contributions from top loops and W loops, respectively, and are expressed in terms of scalar integrals—more specifically, in terms of the Passarino-Veltman two-point integrals B_0 and three-point integrals C_0 [13],

$$S^{\gamma\gamma}_{(T)}(t, m_t^2, m_h^2) = 2 + \frac{2t}{m_h^2 - t}[B_0(m_h^2; m_t^2, m_t^2)$$
$$- B_0(t; m_t^2, m_t^2)] + \{4m_t^2 - m_h^2 + t\}$$
$$\times C_0(m_h^2, 0, t; m_t^2, m_t^2, m_t^2), \qquad (2.6)$$

$$S^{\gamma\gamma}_{(W)}(t, m_W^2, m_h^2) = 6 + \frac{m_h^2 - t}{m_W^2} - \frac{m_h^2 t}{2m_W^4}$$
$$+ \frac{t(12m_W^4 + 2m_W^2(m_h^2 - t) - m_h^2 t)}{2m_W^4(m_h^2 - t)}$$
$$\times [B_0(m_h^2; m_W^2, m_W^2) - B_0(t; m_W^2, m_W^2)]$$
$$+ \left\{ \frac{t(m_h^2 - 2t)}{m_W^2} + 12m_W^2 - 6m_h^2 + 6t \right\}$$
$$\times C_0(m_h^2, 0, t; m_W^2, m_W^2, m_W^2), \qquad (2.7)$$

where m_t and m_W are the top-quark and W-boson masses, respectively. The explicit expressions of the relevant B_0's and C_0's are given in Appendix B. The two-point integrals B_0 have ultraviolet divergences, but the B_0 in Eqs. (2.6) and (2.7) appear in pairs and the differences are finite with the ultraviolet divergences being cancelled out. The integrals C_0 in Eqs. (2.6) and (2.7) are finite. Therefore, $S^{\gamma\gamma}_{(T)}$ and $S^{\gamma\gamma}_{(W)}$ give finite results.

A dimensionless quantity $G_{\gamma\gamma}(t) \equiv F_{\gamma\gamma}(t)/(\frac{t - m_h^2}{2m_W})$ may be considered as a transition form factor of the Higgs boson. In the limit $t \to 0$, $G_{\gamma\gamma}(t)$ reduces to

$$G_{\gamma\gamma}(0) = N_c Q_t^2 F_{1/2} + F_1, \qquad (2.8)$$

where $F_{1/2}$ and F_1 are the top-quark and W-boson loop contributions to the $H \to \gamma\gamma$ decay amplitude [14]. They are given, for example, in Eq. (2.17) of Ref. [15]. The W-boson contribution $|m_W S^{\gamma\gamma}_{(W)}|$ is much larger in magnitude than the top-quark contribution $|\frac{2m_t^2}{m_W} N_c Q_t^2 S^{\gamma\gamma}_{(T)}|$ and grows with $-t$. Thus, $G_{\gamma\gamma}(t)$, the sum of the top-quark and W-boson contributions, grows with $-t$. Actually, it grows as $\log^2 \frac{-t}{m_W^2}$ for large $-t$.

B. Z boson-real photon fusion diagrams

The one-loop $Z^*\gamma$ fusion diagrams for the Higgs boson production are obtained from the one-loop $\gamma^*\gamma$ fusion diagrams given in Figs. 1 and 2 by replacing the photon propagator with that of the Z boson with mass m_Z. Charged fermions and the W boson contribute to the one-loop $Z^*\gamma$ fusion diagrams. Again we only consider the top quark for

the charged fermion loop diagrams. We calculate the contribution from the $Z^*\gamma$ fusion diagrams and obtain,

$$A_{Z\gamma} = \left(\frac{eg^3}{16\pi^2} \right) [\bar{u}(k_1')\gamma_\mu(f_{Ze} + \gamma_5)u(k_1)] \frac{1}{t - m_Z^2}$$
$$\times \left(g^{\mu\beta} - \frac{2k_2^\mu q^\beta}{m_h^2 - t} \right) \epsilon_\beta(k_2) F_{Z\gamma}, \qquad (2.9)$$

with

$$F_{Z\gamma} = - \frac{m_t^2}{8m_W \cos^2\theta_W} N_c Q_t f_{Zt} S^{Z\gamma}_{(T)}(t, m_t^2, m_h^2)$$
$$+ \frac{m_W}{4} S^{Z\gamma}_{(W)}(t, m_W^2, m_h^2), \qquad (2.10)$$

where f_{Ze} and f_{Zt} are the strength of the vector part of the Z-boson coupling to the electron and top quark, respectively, and are given by

$$f_{Ze} = -1 + 4\sin^2\theta_W, \qquad f_{Zt} = 1 - \frac{8}{3}\sin^2\theta_W, \quad (2.11)$$

with θ_W being the Weinberg angle. The axial-vector part of the Z-boson coupling to the top quark [see Eq. (A6)] has a null effect and we find

$$S^{Z\gamma}_{(T)}(t, m_t^2, m_h^2) = S^{\gamma\gamma}_{(T)}(t, m_t^2, m_h^2),$$
$$S^{Z\gamma}_{(W)}(t, m_W^2, m_h^2) = S^{\gamma\gamma}_{(W)}(t, m_W^2, m_h^2). \qquad (2.12)$$

C. "$W\nu_e$" one-loop diagrams

The Feynman diagrams involving the W boson and electron neutrino, which are shown in Fig. 3, also contribute to the Higgs boson production in $e^-\gamma$ collisions. They yield the "$W\nu_e$" amplitude which is written in the following form:

$$A_{W\nu_e} = \left(\frac{eg^3}{16\pi^2} \right) \frac{m_W}{4} [\bar{u}(k_1')F_{(W\nu_e)\beta}(1 - \gamma_5)u(k_1)]\epsilon(k_2)^\beta, \qquad (2.13)$$
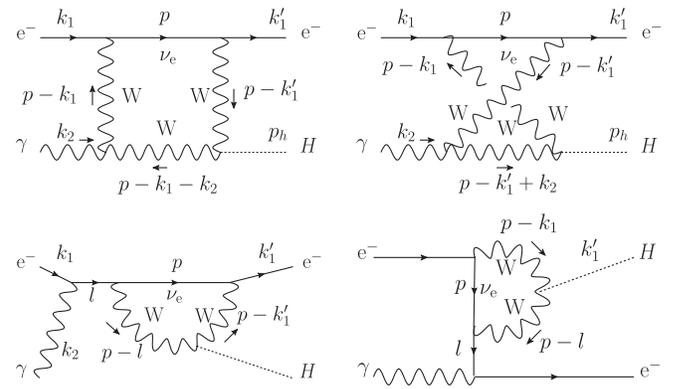

FIG. 3.   "$W\nu_e$" diagrams.

where the factor $(1 - \gamma_5)$ is due to the e-ν-W vertex. Thus, when the electron beams are right-handedly polarized, these "$W\nu_e$" diagrams do not contribute. The factor $F_{(W\nu_e)\beta}$ is written in a gauge-invariant form as

$$F_{(W\nu_e)\beta} = \left(\frac{2k_{1_\beta}k_2}{s} - \gamma_\beta\right) S^{W\nu_e}_{(k_1)}(s, t, m_h^2, m_W^2) + \left(\frac{2k'_{1_\beta}k_2}{u} + \gamma_\beta\right) S^{W\nu_e}_{(k'_1)}(s, t, m_h^2, m_W^2), \tag{2.14}$$

where $S^{W\nu_e}_{(k_1)}$ and $S^{W\nu_e}_{(k'_1)}$ are expressed in terms of the scalar integrals B_0, C_0 and the scalar four-point integrals D_0 as follows:

$$\begin{aligned}
S^{W\nu_e}_{(k_1)}(s, t, m_h^2, m_W^2) =& \frac{(2m_W^2 + m_h^2)s}{2m_W^4(s + u)} + \frac{2}{(s + t)}[B_0(m_h^2; m_W^2, m_W^2) - B_0(u; 0, m_W^2)] \\
&+ \frac{st(2m_W^2 + m_h^2)}{2m_W^4(s + u)^2}[B_0(m_h^2; m_W^2, m_W^2) - B_0(t; m_W^2, m_W^2)] \\
&+ \frac{(m_W^2 - s)}{t}C_0(0, 0, s; m_W^2, m_W^2, 0) - \frac{u(-m_W^2 + s + t)}{st}C_0(0, 0, u; m_W^2, m_W^2, 0) \\
&- \frac{t}{s}C_0(0, 0, t; m_W^2, 0, m_W^2) + \frac{(m_W^2 - s)(t + u)}{st}C_0(0, s, m_h^2; m_W^2, 0, m_W^2) \\
&- \frac{(s^2 - 2st - t^2)(-m_W^2 + s + t)}{st(s + t)}C_0(0, u, m_h^2; m_W^2, 0, m_W^2) \\
&+ \frac{-2m_W^4(s + u)^2 + m_W^2(2s^3 + s^2(3t + 4u) + 2su(t + u) + tu^2) - s^2t(s - t + u)}{m_W^2 st(s + u)} \\
&\times C_0(0, t, m_h^2; m_W^2, m_W^2, m_W^2) \\
&+ \frac{(m_W^2 - s)(m_W^2(s + u) + st)}{st}D_0(0, 0, 0, m_h^2; s, t; m_W^2, m_W^2, 0, m_W^2) \\
&+ \frac{(m_W^4(s + u) - m_W^2(s^2 + s(u - t) + 2tu) + tu(s + t))}{st}D_0(0, 0, 0, m_h^2; t, u; m_W^2, 0, m_W^2, m_W^2), \tag{2.15}
\end{aligned}$$

and

$$\begin{aligned}
S^{W\nu_e}_{(k'_1)}(s, t, m_h^2, m_W^2) =& -\frac{(2m_W^2 + m_h^2)u}{2m_W^4(s + u)} - \frac{2}{(t + u)}[B_0(m_h^2; m_W^2, m_W^2) - B_0(s; 0, m_W^2)] \\
&- \frac{tu(2m_W^2 + m_h^2)}{2m_W^4(s + u)^2}[B_0(m_h^2; m_W^2, m_W^2) - B_0(t; m_W^2, m_W^2)] \\
&+ \frac{s(-m_W^2 + t + u)}{tu}C_0(0, 0, s; m_W^2, m_W^2, 0) - \frac{(m_W^2 - u)}{t}C_0(0, 0, u; m_W^2, m_W^2, 0) \\
&+ \frac{t}{u}C_0(0, 0, t; m_W^2, 0, m_W^2) + \frac{(u^2 - 2tu - t^2)(-m_W^2 + t + u)}{tu(t + u)}C_0(0, s, m_h^2; m_W^2, 0, m_W^2) \\
&- \frac{(m_W^2 - u)(s + t)}{tu}C_0(0, u, m_h^2; m_W^2, 0, m_W^2) \\
&+ \frac{2m_W^4(s + u)^2 - m_W^2(2u^3 + u^2(3t + 4s) + 2su(s + t) + s^2t) + tu^2(s - t + u)}{m_W^2 tu(s + u)} \\
&\times C_0(0, t, m_h^2; m_W^2, m_W^2, m_W^2) \\
&- \frac{(m_W^2 - u)(m_W^2(s + u) + tu)}{tu}D_0(0, 0, 0, m_h^2; t, u; m_W^2, 0, m_W^2, m_W^2) \\
&- \frac{(m_W^4(s + u) - m_W^2(s(2t + u) + u(u - t)) + st(t + u))}{tu}D_0(0, 0, 0, m_h^2; s, t; m_W^2, m_W^2, 0, m_W^2). \tag{2.16}
\end{aligned}$$

The explicit expressions of B_0, C_0 and D_0 are given in Appendix B. The integrals C_0 and D_0 in Eqs. (2.15) and (2.16) are all finite. Again, the integrals B_0 appear in pairs and the differences yield finite results. In the end, $S^{W\nu_e}_{(k_1)}$ and $S^{W\nu_e}_{(k'_1)}$ are finite. Finally we note that $S^{W\nu_e}_{(k'_1)}$ vanishes at $u = 0$, which is anticipated from the expression of the second term in Eq. (2.14).
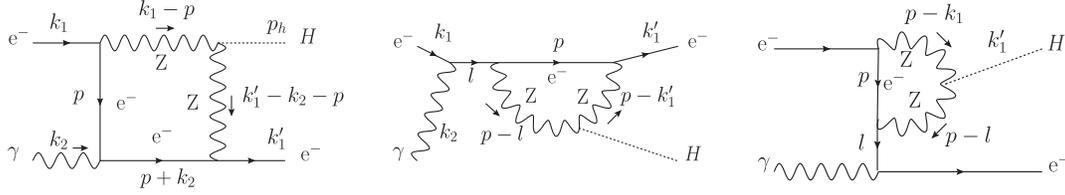
FIG. 4.   "Ze" diagrams.

D. "Ze" one-loop diagrams

The last one-loop contributions to the Higgs boson production in $e^-\gamma$ collisions come from the Feynman diagrams shown in Fig. 4. These "Ze" diagrams give the following amplitude:

$$A_{Ze} = \left(\frac{eg^3}{16\pi^2}\right)\left(-\frac{m_Z}{16\cos^3\theta_W}\right)$$
$$\times [\bar{u}(k_1')F_{(Ze)\beta}(f_{Ze} + \gamma_5)^2 u(k_1)]\epsilon(k_2)^\beta, \quad (2.17)$$

where the factor $(f_{Ze} + \gamma_5)^2$ arises from the Z-boson coupling to electrons. The factor $F_{(Ze)\beta}$ is written in a gauge-invariant form as

$$F_{(Ze)\beta} = \left(\frac{2k_{1_\beta}k_2}{s} - \gamma_\beta\right)S^{Ze}_{(k_1)}(s,t,m_h^2,m_Z^2)$$
$$+ \left(\frac{2k'_{1_\beta}k_2}{u} + \gamma_\beta\right)S^{Ze}_{(k_1')}(s,t,m_h^2,m_Z^2), \quad (2.18)$$

where

$$S^{Ze}_{(k_1)}(s,t,m_h^2,m_Z^2) = -\frac{2}{(s+t)}[B_0(m_h^2;m_Z^2,m_Z^2) - B_0(u;0,m_Z^2)] - \frac{(m_Z^2-s)(t+u)}{st}C_0(0,s,m_h^2;m_Z^2,0,m_Z^2)$$
$$+ \frac{(m_Z^2(-s^2+2st+t^2)+s^3-st^2)}{st(s+t)}C_0(0,u,m_h^2;m_Z^2,0,m_Z^2)$$
$$+ \frac{(m_Z^2-s)}{st}\{sC_0(0,0,s;m_Z^2,0,0) + uC_0(0,0,u;m_Z^2,0,0)$$
$$+ [m_Z^2(s+u)-su]D_0(0,0,0,m_h^2;s,u;m_Z^2,0,0,m_Z^2)\}, \quad (2.19)$$

and

$$S^{Ze}_{(k_1')}(s,t,m_h^2,m_Z^2) = \frac{2}{(t+u)}[B_0(m_h^2;m_Z^2,m_Z^2) - B_0(s;0,m_Z^2)] + \frac{(m_Z^2-u)(s+t)}{tu}C_0(0,u,m_h^2;m_Z^2,0,m_Z^2)$$
$$- \frac{(m_Z^2(t^2+2tu-u^2)-t^2u+u^3)}{tu(t+u)}C_0(0,s,m_h^2;m_Z^2,0,m_Z^2)$$
$$- \frac{(m_Z^2-u)}{tu}\{sC_0(0,0,s;m_Z^2,0,0) + uC_0(0,0,u;m_Z^2,0,0)$$
$$+ [m_Z^2(s+u)-su]D_0(0,0,0,m_h^2;s,u;m_Z^2,0,0,m_Z^2)\}. \quad (2.20)$$

The explicit expressions of the scalar integrals B_0, C_0 and D_0 which appear in Eqs. (2.19) and (2.20) are given in Appendix B. The integrals $C_0(0,s,m_h^2;m_Z^2,0,m_Z^2)$ and $C_0(0,u,m_h^2;m_Z^2,0,m_Z^2)$ are finite. On the other hand, collinear singularities appear in $C_0(0,0,s;m_Z^2,0,0)$, $C_0(0,0,u;m_Z^2,0,0)$ and in the four-point integral $D_0(0,0,0,m_h^2;s,u;m_Z^2,0,0,m_Z^2)$. These collinear divergences

are handled by dimensional regularization. See Eqs. (B28), (B29) and (B37). These scalar integrals with collinear divergences appear in combination as in the parentheses of the last terms of Eqs. (2.19) and (2.20) and, as a result, their collinear divergences cancel out. Thus $S^{Ze}_{(k_1)}$ and $S^{Ze}_{(k_1')}$ are both finite. Note also that $S^{Ze}_{(k_1')}$ vanishes at $u = 0$.

III. HIGGS BOSON PRODUCTION CROSS SECTION

One of the advantages of linear colliders is that we can acquire highly polarized colliding beams. Let us consider the Higgs boson production reaction (2.1) when both the initial electron and photon beams are fully polarized. We denote the polarizations of the electron and photon as $P_e = \pm 1$ and $P_\gamma = \pm 1$, respectively.[2] The differential cross section for $e^- \gamma \to e^- H$ with the initial electron and photon polarizations P_e and P_γ is expressed by,

$$\frac{d\sigma_{(e\gamma \to eH)}(s, P_e, P_\gamma)}{dt} = \frac{1}{16\pi s^2} \times \left\{ \sum_{\text{final electron spin}} |A(P_e, P_\gamma)|^2 \right\}, \quad (3.1)$$

where $A(P_e, P_\gamma)$ is written at the one-loop level as

$$A(P_e, P_\gamma) = A_{\gamma\gamma}(P_e, P_\gamma) + A_{Z\gamma}(P_e, P_\gamma) + A_{W\nu_e}(P_e, P_\gamma) + A_{Ze}(P_e, P_\gamma). \quad (3.2)$$

In the center-of-mass (CM) frame, t and u are expressed as

$$t = -\frac{s - m_h^2}{2}(1 - \cos\theta),$$

$$u = -\frac{s - m_h^2}{2}(1 + \cos\theta), \quad (3.3)$$

where θ is the angle between the initial and scattered electrons. We are dealing with $e^- \gamma$ collisions in the high-energy limit and thus we neglect the electron mass. In the massless limit the helicity of the electron is conserved. Then the angular momentum conservation along the direction of the initial electron requires that the amplitude $A(P_e, P_\gamma)$ should vanish at $\theta = 0$. Hence, apart from the photon propagator which appears as $\frac{1}{t}$, an overall factor t arises in the differential cross section. Also when the electron is scattered in the backward direction, the amplitude $A(P_e, P_\gamma)$ with $P_e P_\gamma = -1$ should vanish at $\theta = \pi$ due to the angular momentum conservation. Hence the differential cross section for the initial beams with $P_e P_\gamma = -1$ vanishes as $u \to 0$ (or $t \to t_{\min} = m_h^2 - s$).

When an initial electron is polarized with polarization P_e, we modify $u(k_1)$ as

$$u(k_1) \to \frac{1 + P_e \gamma_5}{2} u(k_1). \quad (3.4)$$

In the center-of-mass frame where a photon with momentum k_2 is moving in the $+z$ direction, the circular polarization ($P_\gamma = \pm 1$) of the photon is taken to be

$$\epsilon(k_2, \pm 1)_\beta = \frac{1}{\sqrt{2}}(0, \mp 1, -i, 0). \quad (3.5)$$

In this frame, the momenta k_2, k_1 and k_1' are expressed as

$$k_2^\mu = \frac{\sqrt{s}}{2}(1, 0, 0, 1), \qquad k_1^\mu = \frac{\sqrt{s}}{2}(1, 0, 0, -1),$$

$$k_1'^\mu = \frac{s - m_h^2}{\sqrt{s}}(1, \sin\theta\cos\phi, \sin\theta\sin\phi, -\cos\theta), \quad (3.6)$$

and we find that the polarization tensor of the circularly polarized photon is given by

$$\epsilon(k_2, \pm 1)_\alpha^* \epsilon(k_2, \pm 1)_\beta = -\frac{1}{2}g_{\alpha\beta} \pm \frac{i}{2}(g_{\alpha 1}g_{\beta 2} - g_{\alpha 2}g_{\beta 1}). \quad (3.7)$$

With $\varepsilon^{0123} = 1$, we obtain in this frame

$$\{(k_1')^1 \varepsilon^{2\mu\nu\lambda} - (k_1')^2 \varepsilon^{1\mu\nu\lambda}\}k_{1\mu}k_{2\nu}k_{1\lambda}' = -\frac{1}{2}tu,$$

$$\varepsilon^{12\mu\nu}k_{1\mu}k_{1\nu}' = \frac{1}{2}t. \quad (3.8)$$

Using Eqs. (3.4)–(3.8), we evaluate $\sum_{\text{final electron spin}} \times |A(P_e, P_\gamma)|^2$ and obtain the differential cross section for $e^- \gamma \to e^- H$ for each case of polarizations of the electron and photon beams. In order to see the relative contributions from $\gamma^* \gamma$ fusion, $Z^* \gamma$ fusion, and the "$W\nu_e$" and "Ze" diagrams, we evaluate the differential cross section given in Eq. (3.1) by replacing $A(P_e, P_\gamma)$ with $A_{\gamma\gamma}(P_e, P_\gamma)$, $A_{Z\gamma}(P_e, P_\gamma)$, $A_{W\nu_e}(P_e, P_\gamma)$ and $A_{Ze}(P_e, P_\gamma)$, respectively. We obtain

$$\frac{d\sigma_{(\gamma\gamma)}(s, P_e, P_\gamma)}{dt} = \frac{1}{16\pi s^2}\left(\frac{e^3 g}{16\pi^2}\right)^2\left(-\frac{1}{t}\right)F_{\gamma\gamma}^2\left\{\frac{s^2 + u^2}{(s+u)^2} + P_\gamma P_e\left(1 - \frac{2u}{s+u}\right)\right\}, \quad (3.9)$$

$$\frac{d\sigma_{(Z\gamma)}(s, P_e, P_\gamma)}{dt} = \frac{1}{16\pi s^2}\left(\frac{eg^3}{16\pi^2}\right)^2\frac{-t}{(t - m_Z^2)^2}F_{Z\gamma}^2$$
$$\times \left\{(f_{Ze}^2 + 2P_e f_{Ze} + 1)\frac{s^2 + u^2}{(s+u)^2} + P_\gamma(P_e f_{Ze}^2 + 2f_{Ze} + P_e)\left(1 - \frac{2u}{s+u}\right)\right\}, \quad (3.10)$$

---

[2] For the cases of full polarization, we note that $P_e = 2 \times$ electron helicity and $P_\gamma =$ photon helicity.
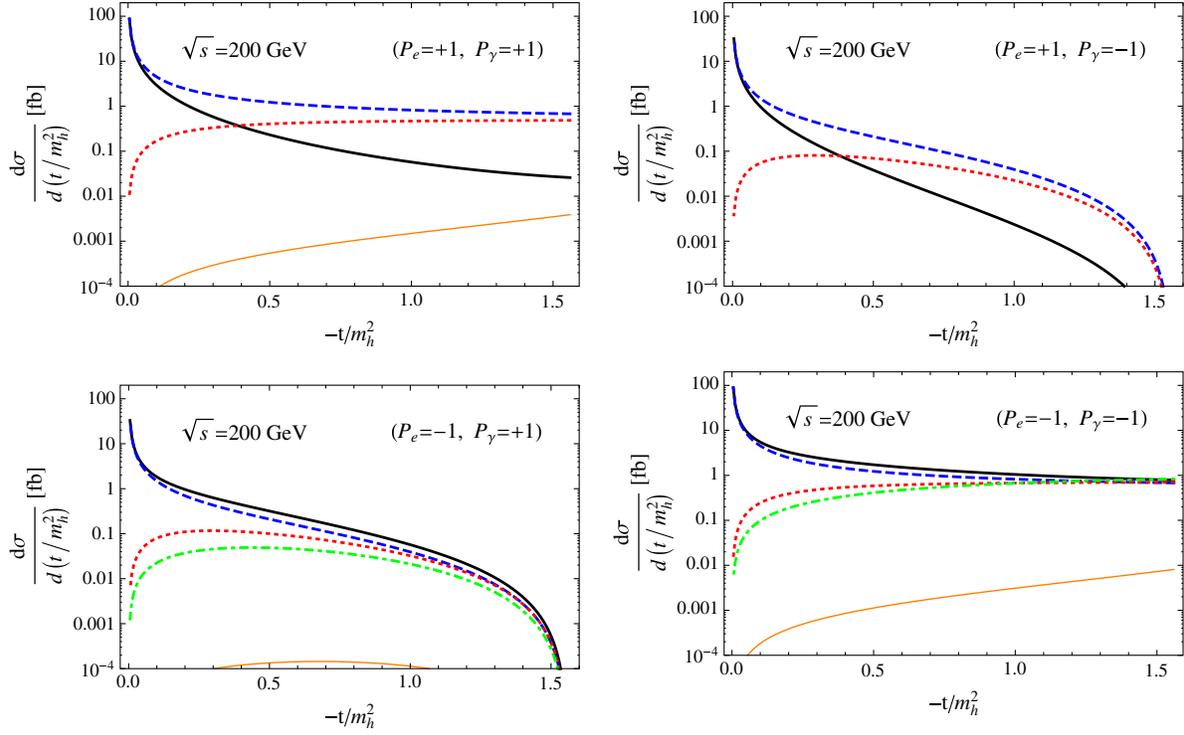
FIG. 5 (color online). The differential cross section for Higgs boson production $d\sigma_{(e\gamma\to eH)}/d(t/m_h^2)$ (black solid line) together with $d\sigma_{(\gamma\gamma)}/d(t/m_h^2)$ (blue dashed line), $d\sigma_{(Z\gamma)}/dt$ (red dotted line), $d\sigma_{(W\nu_e)}/d(t/m_h^2)$ (green dot-dashed line) and $d\sigma_{(Ze)}/d(t/m_h^2)$ (orange thin solid line) as a function of $-t/m_h^2$ with $\sqrt{s} = 200$ GeV for four cases of polarizations of the initial electron and photon beams, $(P_e = +1, P_\gamma = +1)$, $(P_e = +1, P_\gamma = -1)$, $(P_e = -1, P_\gamma = +1)$ and $(P_e = -1, P_\gamma = -1)$. In the plot of $(P_e = +1, P_\gamma = -1)$, $d\sigma_{(Ze)}/dt$ is too small and is out of the plot range.

$$\frac{d\sigma_{(W\nu_e)}(s, P_e, P_\gamma)}{dt} = \frac{1}{16\pi s^2} \left(\frac{eg^3}{16\pi^2}\right)^2 \frac{m_W^2}{8}(-t)(1 - P_e)\{[|S_{(k_1)}^{W\nu_e}(s, t, m_h^2, m_W^2)|^2 + |S_{(k_1')}^{W\nu_e}(s, t, m_h^2, m_W^2)|^2]$$
$$+ P_\gamma[-|S_{(k_1)}^{W\nu_e}(s, t, m_h^2, m_W^2)|^2 + |S_{(k_1')}^{W\nu_e}(s, t, m_h^2, m_W^2)|^2]\}, \tag{3.11}$$

$$\frac{d\sigma_{(Ze)}(s, P_e, P_\gamma)}{dt} = \frac{1}{16\pi s^2} \left(\frac{eg^3}{16\pi^2}\right)^2 \left(\frac{m_Z}{16\cos^3\theta_W}\right)^2 (-t)$$
$$\times \{(f_{Ze}^4 + 4P_e f_{Ze}^3 + 6f_{Ze}^2 + 4P_e f_{Ze} + 1)[|S_{(k_1)}^{Ze}(s, t, m_h^2, m_Z^2)|^2 + |S_{(k_1')}^{Ze}(s, t, m_h^2, m_Z^2)|^2]$$
$$+ P_\gamma(P_e f_{Ze}^4 + 4f_{Ze}^3 + 6P_e f_{Ze}^2 + 4f_{Ze} + P_e)[|S_{(k_1)}^{Ze}(s, t, m_h^2, m_Z^2)|^2$$
$$- |S_{(k_1')}^{Ze}(s, t, m_h^2, m_Z^2)|^2]\}. \tag{3.12}$$

When the initial electron is right-handed ($P_e = +1$), there is no contribution from the "$W\nu_e$" diagrams and we indeed see that $d\sigma(s, P_e = +1, P_\gamma)_{(W\nu_e)}/dt = 0$. Also using the fact that $S_{(k_1')}^{W\nu_e}$ and $S_{(k_1')}^{Ze}$ vanish at $u = 0$, we find that the above four differential cross sections reduce to zero as $u \to 0$ for the case $P_e P_\gamma = -1$. In order to examine the differential cross section for $e^-\gamma \to e^- H$ given in Eq. (3.1), we need to evaluate the interference terms among the four amplitudes $A_{\gamma\gamma}(P_e, P_\gamma)$, $A_{Z\gamma}(P_e, P_\gamma)$, $A_{W\nu_e}(P_e, P_\gamma)$ and

$A_{Ze}(P_e, P_\gamma)$. The expressions of the six interference terms are given in Appendix C.

Now we analyze numerically the differential cross section $d\sigma_{(e\gamma\to eH)}(s, P_e, P_\gamma)/dt$ together with the other four differential cross sections given in Eqs. (3.9)–(3.12). We choose the mass parameters and the coupling constants as follows:

$$m_h = 125 \text{ GeV}, \qquad m_t = 173 \text{ GeV},$$
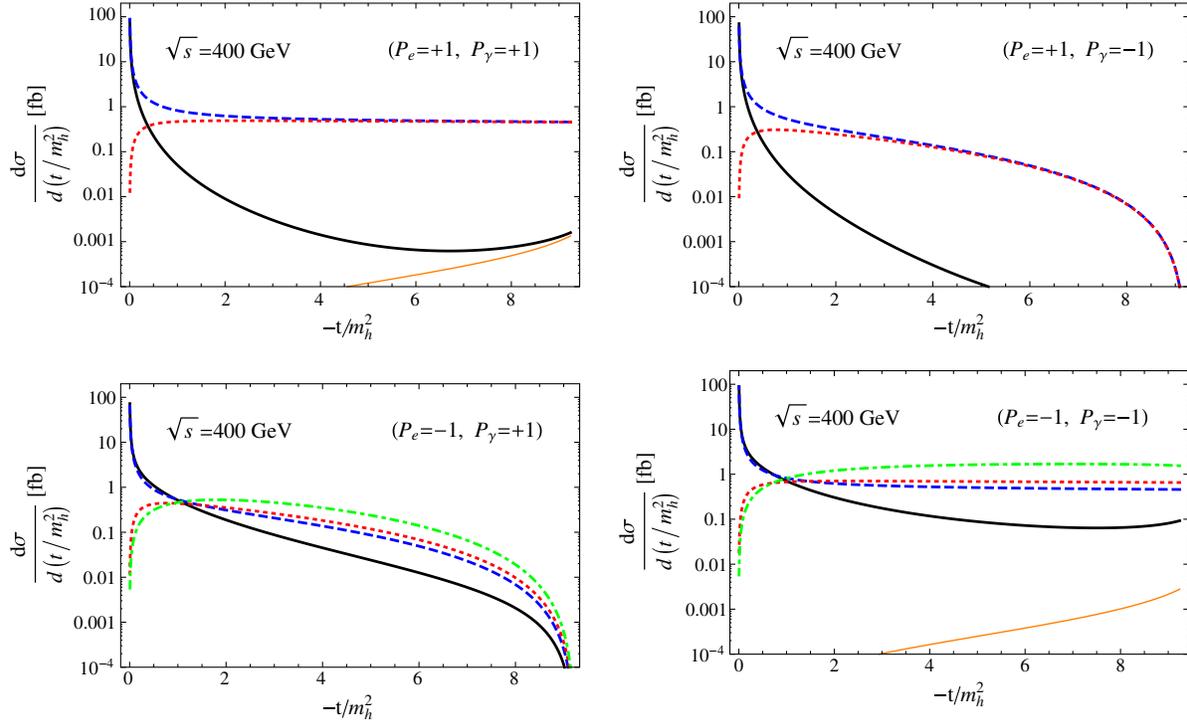$$m_Z = 91 \text{ GeV}, \qquad m_W = 80 \text{ GeV}, \tag{3.13}$$

FIG. 6 (color online).   The differential cross section for Higgs boson production $d\sigma_{(e\gamma\to eH)}/d(t/m_h^2)$ (black solid line) together with $d\sigma_{(\gamma\gamma)}/d(t/m_h^2)$ (blue dashed line), $d\sigma_{(Z\gamma)}/d(t/m_h^2)$ (red dotted line), $d\sigma_{(W\nu_e)}/d(t/m_h^2)$ (green dot-dashed line) and $d\sigma_{(Ze)}/d(t/m_h^2)$ (orange thin solid line) as a function of $-t/m_h^2$ with $\sqrt{s} = 400$ GeV for four cases of polarizations of the initial electron and photon beams, $(P_e = +1, P_\gamma = +1)$, $(P_e = +1, P_\gamma = -1)$, $(P_e = -1, P_\gamma = +1)$ and $(P_e = -1, P_\gamma = -1)$. In the plots of $(P_e = +1, P_\gamma = -1)$ and $(P_e = -1, P_\gamma = +1)$, $d\sigma_{(Ze)}/dt$ is too small and is out of the plot range.

$$\cos\theta_W = \frac{m_W}{m_Z}, \qquad e^2 = 4\pi\alpha_{em} = \frac{4\pi}{128}, \qquad g = \frac{e}{\sin\theta_W}. \tag{3.14}$$

The electromagnetic constant e^2 is chosen to be the value at the scale of m_Z. We plot these differential cross sections as a function of $-t/m_h^2$ in Fig. 5 and Fig. 6 for the cases $\sqrt{s} = 200$ GeV and $\sqrt{s} = 400$ GeV, respectively. The graphs are shown for each case of polarizations of the electron and photon beams. First we find that the contribution from the "Ze" diagrams is very small for all cases compared with those from the other three. Actually, it is negligibly small when $P_e P_\gamma = -1$. In such cases, the terms with dominant $|S_{(k_1)}^{Ze}(s, t, m_h^2, m_Z^2)|^2$ in Eq. (3.12) cancel out and $|S_{(k_1')}^{Ze}(s, t, m_h^2, m_Z^2)|^2$ vanishes as $u \to 0$ (or $t \to t_{\min} = m_h^2 - s$). Also we see that when $P_e P_\gamma = -1$ all the graphs indeed diminish as $u \to 0$.

For the case of polarizations $P_e = -1$ and $P_\gamma = \pm 1$, a dominant contribution at smaller $|t|$, more specifically, up to $-t/m_h^2 = 1$, comes from the $\gamma^*\gamma$ fusion diagrams. This is due to the factor $(-1/t)$ in the expression (3.9) for $d\sigma_{(\gamma\gamma)}/dt$, which arises as $(-t) \times (1/t^2)$ with $1/t$ coming from the photon propagator. For $1 < -t/m_h^2 < 1.5$, the contributions to the differential cross section from $\gamma^*\gamma$

fusion, $Z^*\gamma$ fusion and "$W\nu_e$" diagrams become of the same order, and at $-t/m_h^2 > 1.5$ (see Fig. 6), the contribution of "$W\nu_e$" diagrams prevails over the other two, since "$W\nu_e$" diagrams do not have propagator factors such as $1/t$ and $1/(t - m_Z^2)$. For $P_e = -1$ and $P_\gamma = \pm 1$, the interference between $A_{\gamma\gamma}$ and $A_{Z\gamma}$ works constructively, while the one between $A_{\gamma\gamma}$ and $A_{W\nu_e}$ works destructively and its effect becomes large at $-t/m_h^2 > 1.5$. Thus the values of $d\sigma_{(e\gamma\to eH)}/dt$ become smaller than those of $d\sigma_{(\gamma\gamma)}/dt$, $d\sigma_{(Z\gamma)}/dt$ and $d\sigma_{(W\nu_e)}/dt$ (see Fig. 6).

For the electron polarization $P_e = +1$, no contribution comes from "$W\nu_e$" diagrams. The interference between $A_{\gamma\gamma}$ and $A_{Z\gamma}$ for $P_e = +1$ and $P_\gamma = \pm 1$ works destructively and its effect is large even for small $-t/m_h^2$. Therefore, $d\sigma_{(e\gamma\to eH)}/dt$ decreases rather rapidly as $-t/m_h^2$ increases.

Integrating the differential cross section given in Eq. (3.1) over t, we obtain the Higgs boson production cross section

$$\sigma_{(e\gamma\to eH)}(s, P_e, P_\gamma) = \int_{\text{cut}} dt \, \frac{d\sigma_{(e\gamma\to eH)}(s, P_e, P_\gamma)}{dt}. \tag{3.15}$$

It is known that the forward and backward directions in an $e^-\gamma$ collider are blind spots for the detection of scattered particles. So we set kinematical cuts for the scattered
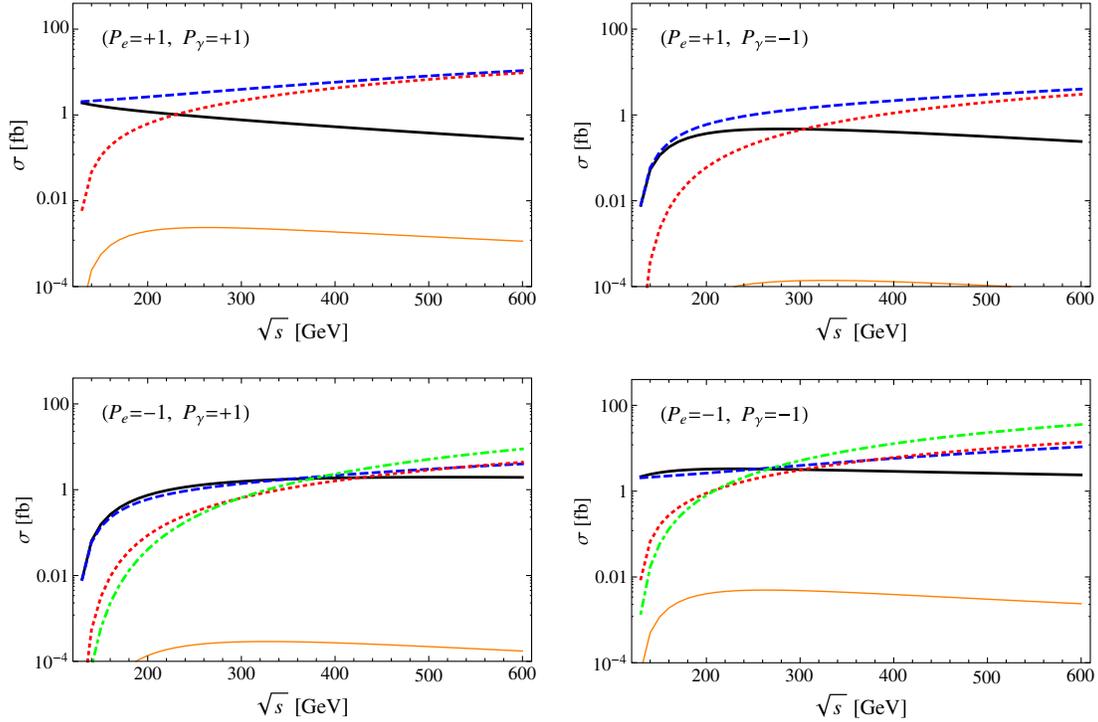
FIG. 7 (color online). Higgs boson production cross section $\sigma_{(e\gamma\to eH)}$ (black solid line), together with $\sigma_{(\gamma\gamma)}$ (blue dashed line), $\sigma_{(Z\gamma)}$ (red dotted line), $\sigma_{(W\nu_e)}$ (green dot-dashed line) and $\sigma_{(Ze)}$ (orange thin solid line) as a function of $\sqrt{s}$ for four cases of polarizations of the initial electron and photon beams, $(P_e = +1, P_\gamma = +1)$, $(P_e = +1, P_\gamma = -1)$, $(P_e = -1, P_\gamma = +1)$ and $(P_e = -1, P_\gamma = -1)$. The kinematical cut is chosen such that the allowed angle θ of the scattered electron in the CM frame is $10° \le \theta \le 170°$.

electron in $e^-\gamma$ collisions. We choose the allowed region of θ in the CM frame given in Eq. (3.3) as $10° \le \theta \le 170°$, which leads to the integration range of t in Eq. (3.15) as $(-s + m_h^2 - t_{cut}) \le t \le t_{cut}$ with $t_{cut} = -\frac{1}{2}(s - m_h^2)\times(1 - \cos 10°)$. We find that the imposition of kinematical cuts reduces the contribution of $\gamma^*\gamma$ fusion diagrams but has almost no effect on the contributions of the other $Z^*\gamma$ fusion, "$W\nu_e$" and "Ze" diagrams.

Similarly we define $\sigma_{(\gamma\gamma)}(s, P_e, P_\gamma)$, $\sigma_{(Z\gamma)}(s, P_e, P_\gamma)$, $\sigma_{(W\nu_e)}(s, P_e, P_\gamma)$ and $\sigma_{(Ze)}(s, P_e, P_\gamma)$ by integrating the expressions given in Eqs. (3.9)–(3.12) over t. We plot these cross sections in Fig. 7 as a function of $\sqrt{s}(\sqrt{s} \ge 130$ GeV) for each case of polarizations of the electron and photon beams. The detailed behaviors of $\sigma_{(e\gamma\to eH)}(s, P_e, P_\gamma)$ in linear scale are summarized in Fig. 8. For the case $P_e P_\gamma = -1$, the Higgs boson production cross section $\sigma_{(e\gamma\to eH)}$ is very small at $\sqrt{s} = 130$ GeV, since the integration range of t is small and the differential cross section vanishes as $t \to t_{min}$. The cross section $\sigma_{(e\gamma\to eH)}(s, P_e = -1, P_\gamma = +1)$ rises gradually up to about 2 fb, while $\sigma_{(e\gamma\to eH)}(s, P_e = +1, P_\gamma = -1)$ increases rather slowly up to 0.4 fb. This is due to the interference between $A_{\gamma\gamma}$ and $A_{Z\gamma}$, which acts constructively for $(P_e = -1, P_\gamma = +1)$ but destructively for $(P_e = +1, P_\gamma = -1)$. For the case $P_e P_\gamma = +1$, the cross section $\sigma_{(e\gamma\to eH)}$ is about 2 fb at $\sqrt{s} = 130$ GeV. The cross section $\sigma_{(e\gamma\to eH)}(s, P_e = -1, P_\gamma = -1)$ rises above 3 fb around

$\sqrt{s} = 200$ GeV and then gradually decreases as $\sqrt{s}$ increases. This is due to the destructive interference between $A_{W\nu_e}$ and $A_{\gamma\gamma}$ and between $A_{W\nu_e}$ and $A_{Z\gamma}$ in the range of large $-t$. Again the destructive interference between $A_{\gamma\gamma}$ and $A_{Z\gamma}$ is responsible for the decrease of $\sigma_{(e\gamma\to eH)}(s, P_e = +1, P_\gamma = +1)$ as $\sqrt{s}$ increases.

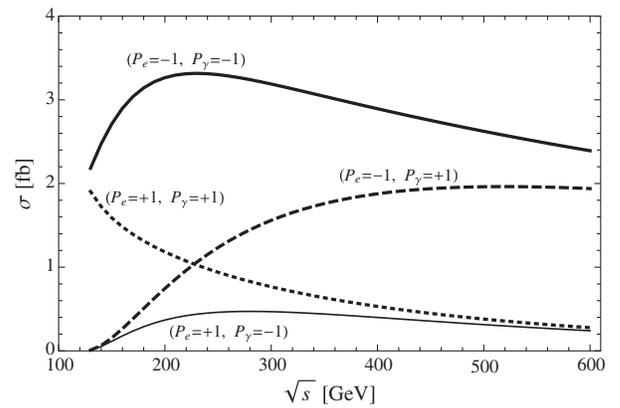
FIG. 8. Higgs boson production cross section $\sigma_{(e\gamma\to eH)}(s, P_e, P_\gamma)$ for the cases of $(P_e = -1, P_\gamma = -1)$ (thick solid line), $(P_e = -1, P_\gamma = +1)$ (dashed line), $(P_e = +1, P_\gamma = +1)$ (dotted line) and $(P_e = +1, P_\gamma = -1)$ (thin solid line). The kinematical cut is chosen such that the allowed angle θ of the scattered electron in the center-of-mass frame is $10° \le \theta \le 170°$.

IV. ANALYSIS OF HIGGS BOSON PRODUCTION IN $e^-\gamma$ COLLISIONS

A high-intensity photon beam can be produced by laser light backward scattering off a high-energy electron beam, $e^-\gamma_{\text{Laser}} \to e^-\gamma$, where the backward-scattered photon receives a major fraction of the incoming electron energy [16]. Its energy distribution depends on the polarizations of the initial electron ($P_{e2} = \pm$) and laser photon ($P_{\text{Laser}} = \pm$). Assuming, for simplicity, that a low-energy laser photon (typically a few eV) has a head-on collision with an electron with high energy (typically 125–250 GeV), we calculate the energy spectra of the scattered photon for different combinations of polarizations of the initial beams and also of the scattered photon. In this situation, the laser photon is scattered backwards and gains a large portion of the electron energy. The energy spectrum of the scattered photon, which is the sum of two helicity states ($P_\gamma = \pm 1$), is given by [17]

$$\frac{1}{\sigma_C}\frac{d\sigma_C}{dy} = \frac{\pi\alpha^2}{2E_{e2}E_{\text{Laser}}\sigma_C}\left[\frac{1}{1-y} + 1 - y - 4r(1-r)\right.$$
$$\left. + P_{e2}P_{\text{Laser}}rx(1-2r)(2-y)\right], \qquad (4.1)$$

where E_{e2} and E_{Laser} are the energies of the initial electron and laser photon, respectively, σ_C is the total cross section of Compton scattering and $y = \frac{\omega}{E_{e2}}$ with ω being the energy of the scattered photon. The variable r is defined as
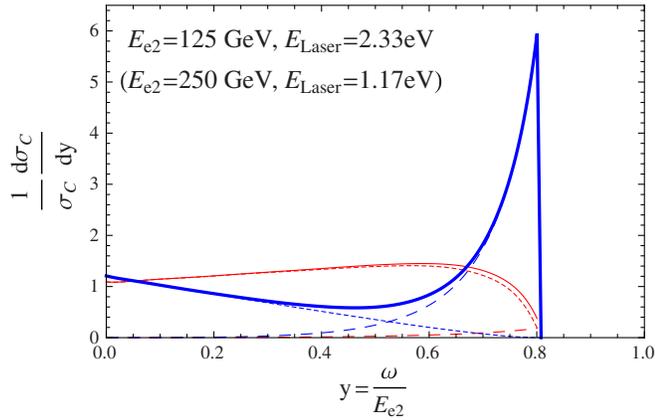

FIG. 9 (color online). The energy spectra of the scattered photons as a function of $y = \frac{\omega}{E_{e2}}$ for the cases of ($E_{\text{Laser}} = 2.33$ eV, $E_{e2} = 125$ GeV) and ($E_{\text{Laser}} = 1.17$ eV, $E_{e2} = 250$ GeV). For both cases, the energy spectra are described by the same graph. The blue and red curves represent the spectra when the initial electron and laser photon have the opposite polarizations ($P_{e2}P_{\text{Laser}} = -1$) and the same polarizations ($P_{e2}P_{\text{Laser}} = +1$), respectively. The dashed and dotted curves show the helicity-flip ($P_\gamma = -P_{\text{Laser}}$) and helicity-non-flip ($P_\gamma = P_{\text{Laser}}$) components of the scattered photon, respectively, and the solid curves represent the sum of the two.

$$r = \frac{y}{x(1-y)}, \qquad \text{with } x = \frac{4E_{e2}E_{\text{Laser}}}{m_e^2}, \qquad (4.2)$$

where m_e is the electron mass. The maximum value of y is given by

$$y_{\text{max}} = \frac{x}{1+x}. \qquad (4.3)$$

The parameter x should be less than 4.83, since the laser photons cannot be too energetic so that the scattered high-energy photons may not disappear by colliding with other laser photons to produce e^+e^- pairs [17]. We assume the use of laser photons with energy 2.33 eV (corresponding to the YAG laser with wavelength 532 nm) for the case of an electron beam with energy 125 GeV and those with energy 1.17 eV (the YAG laser with wavelength 1064 nm) for an electron beam with energy 250 GeV. For both cases we obtain $x = 4.46$ and the energy spectra of the scattered photons are described by the same graph shown in Fig. 9. The solid blue and red curves represent the spectra for the cases when the initial electron and laser photon have the opposite polarizations ($P_{e2}P_{\text{Laser}} = -1$) and the same polarizations ($P_{e2}P_{\text{Laser}} = +1$), respectively. We see from Eq. (4.3) that 82% of the electron energy can be transferred to the scattered photon at the maximum.

Actually we need the energy spectrum for each helicity state P_γ of the scattered photon. We use GRACE [18] to calculate these two helicity components. The result is also shown in Fig. 9. The dashed and dotted (blue and red) curves show the helicity-flip ($P_\gamma = -P_{\text{Laser}}$) and helicity-non-flip ($P_\gamma = P_{\text{Laser}}$) components of the scattered photon, respectively, and the solid curves represent the sum of the two, which are expressed by Eq. (4.1). It is noted that the spectrum with a peak at the kinematic endpoint, $y = y_{\text{max}}$, is obtained when $P_{e2}P_{\text{Laser}} = -1$ (the thick solid blue curve in Fig. 9). The highest-energy photons are produced by the helicity-flip process (the dashed curves) and their helicity P_γ is the opposite of P_{Laser}. Therefore, we are particularly interested in the spectrum for the case $P_{e2}P_{\text{Laser}} = -1$, where the helicity-flipped component dominates the large-y region while helicity-conserved component occupies the small-y region.

Suppose we have a highly polarized e^-e^- collider machine. Converting one of the electron beams to photon beam by means of backward Compton scattering of a polarized laser beam, we obtain an $e^-\gamma$ collider with high polarization. Dividing the energy spectrum of the scattered photon, $\frac{1}{\sigma_C}\frac{d\sigma_C}{dy}$ given in Eq. (4.1), into two pieces $N(y, E_{e2}, E_{\text{Laser}}, P_{e2}, P_{\text{Laser}}, P_\gamma)$ depending on its helicity P_γ, the Higgs boson production cross section for $e^-\gamma \to e^-H$ in an e^-e^- collider, whose beam energies are E_{e1} and E_{e2} and polarizations are P_{e1} and P_{e2}, is expressed as[3]

---

[3]Although, in an actual laser backscattering, the electron and laser beams intersect at a certain angle; here we assume a head-on collision of the two beams and use the energy spectrum of the photon beam obtained by that assumption.

$$\sigma_{e\gamma\text{collision}}(s_{ee}, E_{\text{Laser}}, P_{e1}, P_{e2}, P_{\text{Laser}}) = \sum_{P_\gamma} \int dy N(y, E_{e2}, E_{\text{Laser}}, P_{e2}, P_{\text{Laser}}, P_\gamma) \sigma_{(e\gamma \to eH)}(s, P_{e1}, P_\gamma), \quad (4.4)$$

where $\sigma_{(e\gamma \to eH)}(s, P_{e1}, P_\gamma)$ is given in Eq. (3.15) with P_e replaced by P_{e1}, and s_{ee} is the CM energy squared of the two initial electron beams and is related to s as $s = y s_{ee}$. The integration range of y is given by $y_{\min} \leq y \leq y_{\max}$ with $y_{\min} = 0.25(0.0625)$ for the case $E_{e2}(= E_{e1}) = 125$ GeV (250 GeV).

A feasible channel to observe the SM Higgs boson with mass 125 GeV is $b\bar{b}$ decay, since it has a large branching ratio. We analyze the cross section of the Higgs boson production through the $b\bar{b}$ decay channel, $e + \gamma \to e + H \to e + b + \bar{b}$. The energy spectrum of the photon beam is given by $N(y, E_{e2}, E_{\text{Laser}}, P_{e2}, P_{\text{Laser}}, P_\gamma)$ with $P_{e2}P_{\text{Laser}} = -1$. We consider the two cases (i) $E_{\text{Laser}} = 2.33$ eV, $E_{e2} = 125$ GeV and (ii) $E_{\text{Laser}} = 1.17$ eV, $E_{e2} = 250$ GeV. Both cases give the same spectrum. Note that we take the case $P_{e2}P_{\text{Laser}} = -1$ so that the spectrum has a peak at the highest energy which corresponds to the blue solid curve in Fig. 9. The Monte Carlo method is used. A b-quark mass is chosen to be 4.3 GeV. The angle cuts of the

scattered electron and $b(\bar{b})$ quarks are chosen such that the allowed regions are $10° \leq \theta_{e^-} \leq 170°$ and $10° \leq \theta_{b(\bar{b})} \leq 170°$, respectively, and the energy cuts of these particles are set to be 3 GeV. The Monte Carlo statistical error is about 0.1% when the sampling number is taken to be 200 000.

In Table I we show the results of the Higgs boson production cross section σ_{cut} for the cases $\sqrt{s_{ee}} = 250$ GeV and $\sqrt{s_{ee}} = 500$ GeV and for each combination of polarizations P_{e1} and P_{Laser}. In the case $\sqrt{s_{ee}} = 250$ GeV (and thus $E_{e2} = 125$ GeV), we obtain $y_{\min} = 0.25$, $y_{\max} = 0.82$, and $\sqrt{s_{\max}} \equiv \sqrt{y_{\max} s_{ee}} = 226$ GeV. Hence the cross section $\sigma_{(e\gamma \to eH)}(s, P_{e1}, P_\gamma)$ with $s \leq s_{\max}$ is convolved with the photon energy spectrum in Eq. (4.4). The behaviors of $\sigma_{(e\gamma \to eH)}(s, P_e, P_\gamma)$ for various polarizations P_e and P_γ with $\sqrt{s}$ below 226 GeV which are shown in Fig. 8 and the fact that the helicity-flipped ($P_\gamma = -P_{\text{Laser}}$) component (the dashed blue curve) has a peak at $y = y_{\max}$ and dominates the spectrum region $0.5 < y < y_{\max}$ (see Fig. 9) lead to the expectation

$$\sigma_{\text{cut}}(P_{e1} = -1, P_{\text{Laser}} = 1) > \sigma_{\text{cut}}(P_{e1} = -1, P_{\text{Laser}} = -1)$$
$$> \sigma_{\text{cut}}(P_{e1} = 1, P_{\text{Laser}} = -1) > \sigma_{\text{cut}}(P_{e1} = 1, P_{\text{Laser}} = 1),$$

for $\sqrt{s_{ee}} = 250$ GeV. The Monte Carlo results on σ_{cut} given in Table I confirm our expectation.

On the other hand, the Monte Carlo results for the case $\sqrt{s_{ee}} = 500$ GeV show $\sigma_{\text{cut}}(P_{e1} = -1, P_{\text{Laser}} = -1) > \sigma_{\text{cut}}(P_{e1} = -1, P_{\text{Laser}} = 1)$ and $\sigma_{\text{cut}}(P_{e1} = 1, P_{\text{Laser}} = 1) > \sigma_{\text{cut}}(P_{e1} = 1, P_{\text{Laser}} = -1)$. The changes in the order of the sizes of the cross sections are explained as follows. For $\sqrt{s_{ee}} = 500$ GeV, we obtain $y_{\min} = 0.0625$, $y_{\max} = 0.82$,

TABLE I. Higgs boson production cross section and significance in an $e^- \gamma$ collision in an $e^- e^-$ collider for the cases (i) $E_{\text{Laser}} = 2.33$ eV, $E_{e2} = 125$ GeV, $\sqrt{s_{ee}} = 250$ GeV and (ii) $E_{\text{Laser}} = 1.17$ eV, $E_{e2} = 250$ GeV, $\sqrt{s_{ee}} = 500$ GeV, and for each combination of polarizations P_{e1} and P_{Laser}. P_{e2} is chosen to be $-P_{\text{Laser}}$.

$\sqrt{s_{ee}}$ GeV	P_{e1}	P_{Laser}	σ_{cut} fb	$S/\sqrt{B}$
250	1	−1	0.50	6.17
	1	1	0.36	4.48
	−1	−1	0.80	4.51
	−1	1	1.53	8.68
500	1	−1	0.11	2.93
	1	1	0.19	1.31
	−1	−1	1.22	10.6
	−1	1	1.01	6.8

and $\sqrt{s_{\max}} = 452$ GeV. Figure 9 tells us that the helicity-conserving component (the dotted blue curve) dominates in the small y region, i.e., $y_{\min} \leq y < 0.5$. And we see from Fig. 8 that both $\sigma_{(e\gamma \to eH)}(s, P_e = -1, P_\gamma = -1)$ and $\sigma_{(e\gamma \to eH)}(s, P_e = 1, P_\gamma = 1)$ increase as $\sqrt{s}$ decreases from $\sqrt{s_{\max}}$. These two factors give a concise account of the results on σ_{cut} for $\sqrt{s_{ee}} = 500$ GeV given in Table I.

So far we have considered the cases where both initial electrons and laser photons are fully polarized. Although we can prepare laser photons with full polarization, the electron beams are, in fact, partially polarized. Let us denote the polarization of the incident electrons as

$$p \equiv p_R - p_L \quad (4.5)$$

where p_R is the fraction with positive helicity and $p_L = 1 - p_R$ is the fraction with negative helicity. Now we reconsider the Higgs boson production cross section for $e^- \gamma \to e^- H$ in an $e^- e^-$ collider when the two electron beams have polarizations p_{e1} and p_{e2}. Then Eq. (4.4) is replaced by[4]

---

[4]Note that P_{e1} and P_{e2} take the fixed values ± 1, while p_{e1} and p_{e2} are variables with the range $-1 \leq p_{e1}, p_{e2} \leq 1$.

$$\sigma_{e\gamma \text{ collision}}(s_{ee}, E_{\text{Laser}}, p_{e1}, p_{e2}, P_{\text{Laser}}) = \sum_{P_\gamma} \int dy \left\{ \frac{1 + p_{e2}}{2} N(y, E_{e2}, E_{\text{Laser}}, P_{e2} = +1, P_{\text{Laser}}, P_\gamma) \right.$$

$$+ \frac{1 - p_{e2}}{2} N(y, E_{e2}, E_{\text{Laser}}, P_{e2} = -1, P_{\text{Laser}}, P_\gamma) \Big\}$$

$$\left. \times \left\{ \frac{1 + p_{e1}}{2} \sigma_{(e\gamma \to eH)}(s, P_{e1} = +1, P_\gamma) + \frac{1 - p_{e1}}{2} \sigma_{(e\gamma \to eH)}(s, P_{e1} = -1, P_\gamma) \right\}. \quad (4.6)$$

For example, setting $p_{e1} = p_{e2} = -0.8$ [19] and $P_{\text{Laser}} = +1$, we obtain $\sigma_{\text{cut}} = 1.28$ fb and 0.92 fb, respectively, for the cases $\sqrt{s_{ee}} = 250$ GeV and $\sqrt{s_{ee}} = 500$ GeV. Particularly, here we have chosen a negative polarization for p_{e1}. This is in order to increase the contribution from the "$W\nu_e$" one-loop diagrams.

We also analyze the significance $S/\sqrt{B}$ of the Higgs boson production in $e^-\gamma$ collisions. The $b\bar{b}$ decay channel of the Higgs boson in $e^-\gamma$ collisions has a substantial background. Two examples of the background processes are shown in Fig. 10.

In particular, a huge background appears at the Z-boson pole. However, it is expected that when we measure the invariant mass $m_{b\bar{b}}$ of b and $\bar{b}$ quarks, the background will be small in the region $m_{b\bar{b}} > 120$ GeV compared with the signals of the Higgs boson production. We use GRACE to write down all the tree Feynman diagrams for $e + \gamma \to e + b + \bar{b}$ and to evaluate their contributions to the background cross section. We assume that the integrated luminosity is 250 fb^{-1}. The significance is calculated by taking samples in the region 120 GeV $\leq m_{b\bar{b}} \leq$ 130 GeV at the parton level. The results are given in Table I. Large values of the significance are obtained for the cases of $(P_{e1}, P_{\text{Laser}}) = (1, -1)$ and $(-1, 1)$ with $\sqrt{s_{ee}} = 250$ GeV and $(P_{e1}, P_{\text{Laser}}) = (-1, \mp 1)$ with $\sqrt{s_{ee}} = 500$ GeV.

An additional background to the reaction $e + \gamma \to e + H \to e + b + \bar{b}$ is the resolved photon process $e + \gamma(g) \to e + b + \bar{b}$, where the gluon content in a photon interacts with γ (and also Z) to produce a $b\bar{b}$ pair. This background process was considered in Refs. [10,11]. We estimate this background as follows. The gluon content in a photon has not been reliably measured until now and parametrizations of the gluon distribution have been proposed only for the case of an unpolarized photon in the literature [20,21]. Therefore, we study both the resolved photon process $e + \gamma(g) \to e + b + \bar{b}$ and the direct photon process $e + \gamma \to e + b + \bar{b}$ in an e^-e^- collider for the
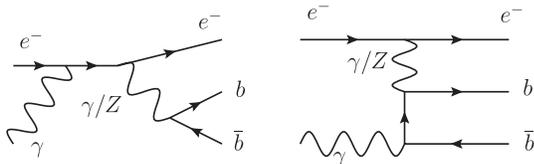
case when initial electron beams and laser photons are unpolarized. We use the gluon distribution function $f_{G/\gamma}(z, Q^2)$ in an unpolarized photon given by the parametrization in Ref. [21], where Q^2 is the scale at which the structure of the photon is being probed and z is the fraction of the photon energy carried by the gluon. The cross section for $e + \gamma(g) \to e + b + \bar{b}$ is expressed as

$$\int_0^{y_{\text{max}}} dy N_{\text{unpol}}(y, E_{e2}, E_{\text{laser}})$$

$$\times \int_0^1 dz f_{G/\gamma}(z, Q^2) \sigma(eg \to eb\bar{b})(zys_{ee}) \quad (4.7)$$

where $N_{\text{unpol}}(y, E_{e2}, E_{\text{laser}}) = \frac{1}{\sigma_C} \frac{d\sigma_C}{dy}\big|_{\text{unpol}}$ which is obtained from Eq. (4.1) by setting $P_{e2} P_{\text{Laser}} = 0$. Again we use GRACE to write down all the tree Feynman diagrams for $e + g \to e + b + \bar{b}$ and to evaluate the cross section $\sigma(eg \to eb\bar{b})$. We choose Q^2 as $-(k_1 - k_1')^2 = -t$ for $f_{G/\gamma}(z, Q^2)$ and also for the running strong coupling constant $\alpha_s(Q^2)$. Since the gluon content in a photon accumulates in a small-z region, the invariant mass $m_{b\bar{b}}$ distribution of the resolved photon background cross section is expected to become smaller as $m_{b\bar{b}}$ gets large. It is also noted that in the direct photon process, the effect of the Z-boson pole (see the left diagram in Fig. 10) on the background cross section remains to some extent as a tail in the region $m_{b\bar{b}} = 125$ GeV, but that in the resolved photon process, there is no such Z-boson pole effect. We obtain 0.06 for the background ratio of $d\sigma_{\text{cut}}/dm_{b\bar{b}}$ between the resolved photon and direct photon processes at $m_{b\bar{b}} = 125$ GeV in the case $\sqrt{s_{ee}} = 500$ GeV. When $\sqrt{s_{ee}} = 250$ GeV, the ratio becomes negligibly small. Hence we find that the contribution of the resolved photon process to the background is very small compared to that of the direct photon process when we observe a pair of $b\bar{b}$ at the invariant mass around $m_{b\bar{b}} = 125$ GeV. Although the analysis so far was on the background contributions for the case of the unpolarized beams, we expect that the same trend still remains when we use the polarized electron and photon beams.

Due to the electric charge factors, $c\bar{c}$ pairs have larger production cross sections than $b\bar{b}$ pairs. If the $c\bar{c}$ pairs are misidentified as $b\bar{b}$, they turn out to be a further background for the reaction $e + \gamma \to e + H \to e + b + \bar{b}$. This is a reducible background and can be controllable if we have a detector with good efficiency for b identification and
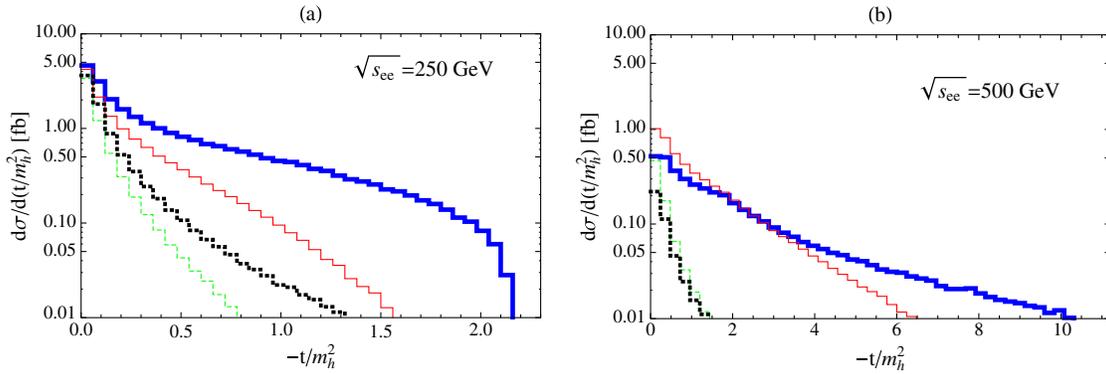

FIG. 10. Examples of background processes for $e + \gamma \to e + b + \bar{b}$.

FIG. 11 (color online). Monte Carlo results for the differential cross section $d\sigma_{\mathrm{cut}}/d(t/m_h^2)$ for the process $e\gamma \to eH \to e(b\bar{b})$ in $e^-\gamma$ collision in an e^-e^- collider for the cases (a) $\sqrt{s_{ee}} = 250$ GeV and (b) $\sqrt{s_{ee}} = 500$ GeV. The blue thick, red thin, black thick dashed and green thin dashed lines represent the results for the cases where $(P_{e1}, P_{\mathrm{Laser}})$ are $(-1, 1)$, $(-1, -1)$, $(1, -1)$ and $(1,1)$, respectively, and $P_{e2} = -P_{\mathrm{Laser}}$.

c rejection. We compute the rate for $e + \gamma \to e + c + \bar{c}$ in an e^-e^- collider for the case of the unpolarized electron and photon beams. We find that $d\sigma_{\mathrm{cut}}(e\gamma \to ec\bar{c})/dm_{c\bar{c}}$ is larger than $d\sigma_{\mathrm{cut}}(e\gamma \to eb\bar{b})/dm_{b\bar{b}}$ at $m_{c\bar{c}} = m_{b\bar{b}} = 125$ GeV by a factor of 3.2 (3.1) when $\sqrt{s_{ee}} = 250$ GeV ($\sqrt{s_{ee}} = 500$ GeV). The effect of electric charge difference, $Q_c = \frac{2}{3}$ and $Q_b = -\frac{1}{3}$, does not appear as significant as we have expected. The reason is that, as mentioned above, at the invariant mass of 125 GeV, the contribution from the diagrams with a Z-boson propagator also becomes important. Thus this reducible background $e\gamma \to ec\bar{c}$ will be brought under control once we prepare for a detector with a good b-tagging efficiency.

After all, we conclude that the Higgs boson will be clearly observed in $e^-\gamma$ collision experiments.

Finally we show the results of our Monte Carlo analysis on the differential cross section $d\sigma_{\mathrm{cut}}/d(t/m_h^2)$ for the process $e\gamma \to eH \to e(b\bar{b})$ in $e^-\gamma$ collision in an e^-e^- collider. In Fig. 11 we plot $d\sigma_{\mathrm{cut}}/d(t/m_h^2)$ as a function of $-t/m_h^2$ for the cases (a) $\sqrt{s_{ee}} = 250$ GeV and (b) $\sqrt{s_{ee}} = 500$ GeV, and for each combination of polarizations P_{e1} and P_{Laser}. The kinematical cuts are the same as before. The behaviors of the four differential cross sections in Fig. 11(a) are consistent with the observation that, for $\sqrt{s_{ee}} = 250$ GeV, the helicity-flipped ($P_\gamma = -P_{\mathrm{Laser}}$) component dominates the photon spectrum and with the results on $d\sigma_{(e\gamma \to eH)}/d(t/m_h^2)$ (black solid lines) for $\sqrt{s} = 200$ GeV in Fig. 5. Also these four differential cross sections are in conformity with the numerical values of $\sigma_{\mathrm{cut}}(\mathrm{fb})$ for $\sqrt{s_{ee}} = 250$ GeV in Table I. In the case $\sqrt{s_{ee}} = 500$ GeV, the lower region of y, i.e., $0.0625 < y < 0.5$ where the helicity-conserving component dominates the photon spectrum, participates in the convolution integral in Eq. (4.4) as well. Together with the results on $d\sigma_{(e\gamma \to eH)}/d(t/m_h^2)$ (black solid lines) for $\sqrt{s} = 400$ GeV in Fig. 6, this explains the behaviors of the four differential cross sections in Fig. 11(b). The crossover of the blue thick ($P_{e1} = -1, P_{\mathrm{Laser}} = 1$) and red thin

$(P_{e1} = -1, P_{\mathrm{Laser}} = -1)$ lines near $-t/m_h^2 = 3$ gives an account of the change in the order of the size for σ_{cut} in Table I. We see a sharp drop of $d\sigma_{\mathrm{cut}}/d(t/m_h^2)$ for the case $P_{e1} = 1$ [see the black thick dashed and green thin dashed lines in Figs. 11(a) and 11(b)]. This is due to the fact that, for the case $P_{e1} = 1$, no contribution comes from "$W\nu_e$" diagrams and the interference between $\gamma^*\gamma$ and $Z^*\gamma$ fusion diagrams works destructively.

In Ref. [9], we have pointed out the transition form factor of the Higgs boson via $\gamma^*\gamma$ fusion and its feasibility of observation in $e^-\gamma$ collision experiments. In Table I we see rather large significances for both $\sqrt{s_{ee}} = 250$ GeV and $\sqrt{s_{ee}} = 500$ GeV in the case of $P_{e1} = -1$. See also the blue and red plots in Figs. 11(a) and 11(b). As regards the differential cross section for the Higgs boson production, we find that the contribution of $\gamma^*\gamma$ fusion diagrams is dominant up to $-t/m_h^2 = 1$ for the case of $P_{e1} = -1$. Hence we conclude that when the left-handed electron beam is used, the transition form factor of the Higgs boson is measurable and extracted from the differential cross section for the Higgs boson production up to $-t/m_h^2 = 1$.

V. SUMMARY

We have investigated the SM Higgs boson production in $e^-\gamma$ collisions. The electroweak one-loop contributions to the scattering amplitude for $e^-\gamma \to e^-H$ were calculated and they were expressed in analytical form. Since large polarizations for the initial beams can be obtained in linear colliders, we analyzed both the differential cross section $d\sigma_{(e\gamma \to eH)}(s, P_e, P_\gamma)/dt$ and the cross section $\sigma_{(e\gamma \to eH)}(s, P_e, P_\gamma)$ for each combination of polarizations of the electron and photon beams. We have found the following. (i) Both the differential cross section and cross section are significantly dependent on the polarizations of the electron and photon beams. (ii) The interferences between $\gamma^*\gamma$ and $Z^*\gamma$ fusion diagrams and between $\gamma^*\gamma$ fusion and "$W\nu_e$" diagrams, which work destructively or constructively depending on the polarizations of the initial

beams, are important factors affecting the behaviors of both the differential cross section and cross section. (iii) For $P_e = -1$, the contribution to $d\sigma_{(e\gamma \to eH)}/dt$ from $\gamma^*\gamma$ fusion diagrams is dominant for $-t/m_h^2 \lesssim 1$. Thus the transition form factor of the Higgs boson is measurable and extracted from the differential cross section for the Higgs boson production up to $-t/m_h^2 = 1$, when the left-handed electron beam is used. (iv) The "$W\nu_e$" diagrams do not contribute to the reaction $e^-\gamma \to e^-H$ for $P_e = +1$. But they take part in the reaction for $P_e = -1$, together with the $\gamma^*\gamma$ fusion and $Z^*\gamma$ fusion diagrams. (v) The contribution from "Ze" diagrams is extremely small and can be negligible.

We analyzed the cross section of the Higgs boson production through the $b\bar{b}$ decay channel, $e + \gamma \to e + H \to e + b + \bar{b}$, in an $e^-\gamma$ collision in an e^-e^- collider. A high-energy photon beam was assumed to be produced by laser light backward scattering off one of the high-energy electron beams of the e^-e^- collider. We obtained large values of the significance $\sqrt{S}/B$ for the Higgs boson production for both $\sqrt{s_{ee}} = 250$ GeV and $\sqrt{s_{ee}} = 500$ GeV. We therefore conclude that the Higgs boson will be clearly observed in $e^-\gamma$ collision experiments.

As a final comment, we point out that in an $e^-\gamma$ collider, the photon structure functions can be measured by the single electron-tagging experiments. Analyses of photon structure functions have been intensively performed by using perturbative QCD [22].

APPENDIX A: FEYNMAN RULES

The W- and Z-boson propagators in unitary gauge are, respectively, given by

$$\frac{-i}{k^2 - m_W^2}\left(g_{\mu\nu} - \frac{k_\mu k_\nu}{m_W^2}\right), \qquad \frac{-i}{k^2 - m_Z^2}\left(g_{\mu\nu} - \frac{k_\mu k_\nu}{m_Z^2}\right). \tag{A1}$$

The Feynman rules for the tree-point and four-point vertices are

$$e \cdot e \cdot \gamma \text{ vertex} : i(-e)\gamma_\mu, \tag{A2}$$

$$t \cdot t \cdot \gamma \text{ vertex} : i(Q_t e)\gamma_\mu, \tag{A3}$$

$$e \cdot \nu \cdot W \text{ vertex} : i\frac{g}{2\sqrt{2}}\gamma_\mu(1 - \gamma_5), \tag{A4}$$

$$e \cdot e \cdot Z \text{ vertex} : i\frac{g}{4\cos\theta_W}\gamma_\mu(f_{Ze} + \gamma_5) \quad \text{with} \quad f_{Ze} = -1 + 4\sin^2\theta_W, \tag{A5}$$

$$t \cdot t \cdot Z \text{ vertex} : i\frac{g}{4\cos\theta_W}\gamma_\mu[f_{Zt} - \gamma_5] \quad \text{with} \quad f_{Zt} = 1 - \frac{8}{3}\sin^2\theta_W, \tag{A6}$$

$$\text{Higgs} \cdot t \cdot t \text{ vertex} : -i\frac{gm_t}{2m_W}, \tag{A7}$$

$$\text{Higgs} \cdot W \cdot W \text{ vertex} : igm_W g_{\mu\nu}, \tag{A8}$$

$$\text{Higgs} \cdot Z \cdot Z \text{ vertex} : i\frac{gm_Z}{\cos\theta_W}g_{\mu\nu}, \tag{A9}$$

$$A_\mu(k_1) \cdot W_\nu^+(k_2) \cdot W_\lambda^-(k_3) \text{ vertex} : -ie[(k_1 - k_2)_\lambda g_{\mu\nu} + (k_2 - k_3)_\mu g_{\nu\lambda} + (k_3 - k_1)_\nu g_{\lambda\mu}], \tag{A10}$$

$$Z_\mu(k_1) \cdot W_\nu^+(k_2) \cdot W_\lambda^-(k_3) \text{ vertex} : -ig\cos\theta_W[(k_1 - k_2)_\lambda g_{\mu\nu} + (k_2 - k_3)_\mu g_{\nu\lambda} + (k_3 - k_1)_\nu g_{\lambda\mu}], \tag{A11}$$

$$A_\mu \cdot A_\nu \cdot W_\alpha^+ \cdot W_\beta^- \text{ vertex} : -ie^2[2g_{\mu\nu}g_{\alpha\beta} - g_{\mu\alpha}g_{\nu\beta} - g_{\mu\beta}g_{\nu\alpha}], \tag{A12}$$

$$A_\mu \cdot Z_\nu \cdot W_\alpha^+ \cdot W_\beta^- \text{ vertex} : -ieg\cos\theta_W[2g_{\mu\nu}g_{\alpha\beta} - g_{\mu\alpha}g_{\nu\beta} - g_{\mu\beta}g_{\nu\alpha}], \tag{A13}$$

where, in Eqs. (A10) and (A11), momenta are all inward.

APPENDIX B: SCALAR ONE-LOOP INTEGRALS

The scalar one-loop integrals which appeared in Sec. II are the two-, three- and four-point integrals which are defined as

$$B_0(p^2; m_1^2, m_2^2) \equiv \frac{(2\pi\mu)^{4-n}}{i\pi^2} \int \frac{d^n k}{[k^2 - m_1^2][(k+p)^2 - m_2^2]}, \tag{B1}$$

$$C_0(p_1^2, p_2^2, p_3^2; m_1^2, m_2^2, m_3^2) \equiv \frac{(2\pi\mu)^{4-n}}{i\pi^2} \int \frac{d^n k}{[k^2 - m_1^2][(k+p_1)^2 - m_2^2][(k+p_1+p_2)^2 - m_3^2]}, \tag{B2}$$

$$D_0(p_1^2, p_2^2, p_3^2, p_4^2; s_{12}, s_{23}; m_1^2, m_2^2, m_3^2, m_4^2) \equiv \frac{(2\pi\mu)^{4-n}}{i\pi^2} \int \frac{d^n k}{[k^2 - m_1^2][(k+p_1)^2 - m_2^2][(k+p_1+p_2)^2 - m_3^2][(k-p_4)^2 - m_4^2]}, \tag{B3}$$

where $n = 4 - 2\epsilon$ and μ is the mass scale of dimensional regularization. Note that $p_1 + p_2 + p_3 = 0$ for the three-point function C_0 and $p_1 + p_2 + p_3 + p_4 = 0$ for the four-point function D_0. We evaluate these integrals for the case of the parameters s, t, u, m_h^2, m_W^2 and m_Z^2 which satisfy the following kinematical constraints:

$$s > m_h^2, \qquad -(s - m_h^2) \le t \le 0, \qquad -(s - m_h^2) \le u \le 0,$$
$$m_h^2 < 4m_W^2, \qquad m_h^2 < 4m_Z^2. \tag{B4}$$

Therefore, analytic continuation is necessary for the variable s from $s < 0$ to $s > m_h^2$.

The integrals are expressed in terms of the following ratios:

$$t_T \equiv \frac{t}{m_t^2}, \qquad h_T \equiv \frac{m_h^2}{m_t^2}, \tag{B5}$$

$$s_W \equiv \frac{s}{m_W^2}, \qquad t_W \equiv \frac{t}{m_W^2}, \qquad u_W \equiv \frac{u}{m_W^2}, \qquad h_W \equiv \frac{m_h^2}{m_W^2}, \tag{B6}$$

$$s_Z \equiv \frac{s}{m_Z^2}, \qquad t_Z \equiv \frac{t}{m_Z^2}, \qquad u_Z \equiv \frac{u}{m_Z^2}, \qquad h_Z \equiv \frac{m_h^2}{m_Z^2}. \tag{B7}$$

1. Two-point integrals

The ultraviolet divergences appear in the scalar two-points integrals B_0 and they are expressed by the $\frac{1}{\epsilon}$ terms in dimensional regularization. But when we take difference between two B_0's, the result becomes finite. Specifically we obtain

$$B_0(m_h^2; m_t^2, m_t^2) - B_0(t; m_t^2, m_t^2) = -2\sqrt{\frac{4}{h_T} - 1} \sin^{-1}\left(\sqrt{\frac{h_T}{4}}\right) + \sqrt{1 - \frac{4}{t_T}} \log\left(\frac{\sqrt{4 - t_T} + \sqrt{-t_T}}{\sqrt{4 - t_T} - \sqrt{-t_T}}\right), \tag{B8}$$

$$B_0(s; 0, m_W^2) - B_0(0; m_W^2, m_W^2) = 2 + \left(\frac{1}{s_W} - 1\right)\{\log(s_W - 1) - i\pi\}, \tag{B9}$$

$$B_0(u; 0, m_W^2) - B_0(0; m_W^2, m_W^2) = 2 + \left(\frac{1}{u_W} - 1\right)\log(1 - u_W), \tag{B10}$$

$$B_0(t; m_W^2, m_W^2) - B_0(0; m_W^2, m_W^2) = 2 - \sqrt{1 - \frac{4}{t_W}} \log\left(\frac{\sqrt{4 - t_W} + \sqrt{-t_W}}{\sqrt{4 - t_W} - \sqrt{-t_W}}\right), \tag{B11}$$

$$B_0(m_h^2; m_W^2, m_W^2) - B_0(0; m_W^2, m_W^2) = 2 - 2\sqrt{\frac{4}{h_W} - 1}\sin^{-1}\left(\sqrt{\frac{h_W}{4}}\right), \tag{B12}$$

$$B_0(s; 0, m_Z^2) - B_0(0; 0, m_Z^2) = 1 + \left(\frac{1}{s_Z} - 1\right)\{\log(s_Z - 1) - i\pi\}, \tag{B13}$$

$$B_0(u; 0, m_Z^2) - B_0(0; 0, m_Z^2) = 1 + \left(\frac{1}{u_Z} - 1\right)\log(1 - u_Z), \tag{B14}$$

$$B_0(m_h^2; m_Z^2, m_Z^2) - B_0(0; 0, m_Z^2) = 1 - 2\sqrt{\frac{4}{h_Z} - 1}\sin^{-1}\left(\sqrt{\frac{h_Z}{4}}\right). \tag{B15}$$

2. Three-point integrals

We introduce the following parameters:

$$\lambda_1 \equiv \frac{1}{2}\left(1 - \sqrt{1 - \frac{4}{t_W}}\right), \qquad \lambda_2 \equiv \frac{1}{2}\left(1 + \sqrt{1 - \frac{4}{t_W}}\right), \tag{B16}$$

$$x_{W_+} \equiv \frac{1}{2}\left(1 + i\sqrt{\frac{4}{h_W} - 1}\right), \qquad x_{W_-} \equiv \frac{1}{2}\left(1 - i\sqrt{\frac{4}{h_W} - 1}\right), \tag{B17}$$

$$x_{Z_+} \equiv \frac{1}{2}\left(1 + i\sqrt{\frac{4}{h_Z} - 1}\right), \qquad x_{Z_-} \equiv \frac{1}{2}\left(1 - i\sqrt{\frac{4}{h_Z} - 1}\right). \tag{B18}$$

The three-point integrals given below are all finite except for the last two.

$$C_0(m_h^2, 0, t; m_t^2, m_t^2, m_t^2) = \frac{1}{t - m_h^2}\left\{\frac{1}{2}\log^2\left(\frac{\sqrt{4 - t_T} + \sqrt{-t_T}}{\sqrt{4 - t_T} - \sqrt{-t_T}}\right) + 2\left[\sin^{-1}\sqrt{\frac{h_T}{4}}\right]^2\right\}, \tag{B19}$$

$$C_0(0, 0, s; m_W^2, m_W^2, 0) = \frac{1}{s}\left\{\mathrm{Li}_2\left(\frac{1}{s_W}\right) + \frac{1}{2}(\log(s_W) - i\pi)^2 + \frac{\pi^2}{6}\right\}, \tag{B20}$$

$$C_0(0, 0, u; m_W^2, m_W^2, 0) = -\frac{1}{u}\mathrm{Li}_2(u_W), \tag{B21}$$

$$C_0(0, 0, t; m_W^2, 0, m_W^2) = \frac{-1}{t}\left\{\mathrm{Li}_2(t_W) + \mathrm{Li}_2\left(\frac{1}{\lambda_1}\right) + \mathrm{Li}_2\left(\frac{1}{\lambda_2}\right) - \mathrm{Li}_2\left(-\frac{\lambda_2}{\lambda_1^2}\right) - \mathrm{Li}_2\left(-\frac{\lambda_1}{\lambda_2^2}\right)\right.$$
$$\left. + 4\log\left(-\sqrt{-t_W}\lambda_1\right)\log(1 - \lambda_2 t_W)\right\}, \tag{B22}$$

$$C_0(0, s, m_h^2; m_W^2, 0, m_W^2) = \frac{-1}{s - m_h^2}\left\{ \text{Li}_2\left(\frac{1}{(s_W - h_W)x_{W_+} + 1}\right) + \text{Li}_2\left(\frac{1}{(s_W - h_W)x_{W_-} + 1}\right)\right.$$

$$- \text{Li}_2\left(\frac{s_W - h_W + 1}{(s_W - h_W)x_{W_+} + 1}\right) - \text{Li}_2\left(\frac{s_W - h_W + 1}{(s_W - h_W)x_{W_-} + 1}\right)$$

$$- \text{Li}_2(h_W - s_W) + \text{Li}_2\left(\frac{(s_W - 1)(s_W - h_W)}{s_W^2 - h_W s_W + h_W}\right) - \text{Li}_2\left(\frac{h_W - s_W}{s_W^2 - h_W s_W + h_W}\right)$$

$$+ \log(s_W - h_W + 1)\log\left(\frac{s_W^2 - s_W h_W + h_W}{(s_W - h_W)^2}\right)$$

$$\left. + \log(s_W - 1)\log\left(\frac{s_W}{s_W^2 - s_W h_W + h_W}\right) + i\pi\log\left(\frac{s_W^2 - s_W h_W + h_W}{s_W}\right)\right\}, \qquad (B23)$$

$$C_0(0, u, m_h^2; m_W^2, 0, m_W^2) = \frac{-1}{u - m_h^2}\left\{ \text{Li}_2\left(\frac{1}{1 + (u_W - h_W)x_{W_+}}\right) + \text{Li}_2\left(\frac{1}{1 + (u_W - h_W)x_{W_-}}\right)\right.$$

$$- \text{Li}_2\left(\frac{u_W - h_W + 1}{1 + (u_W - h_W)x_{W_+}}\right) - \text{Li}_2\left(\frac{u_W - h_W + 1}{1 + (u_W - h_W)x_{W_-}}\right) + \text{Li}_2(u_W - h_W + 1)$$

$$\left. - \text{Li}_2\left(\frac{u_W}{u_W^2 - h_W u_W + h_W}\right) + \text{Li}_2\left(\frac{u_W(u_W - h_W + 1)}{u_W^2 - h_W u_W + h_W}\right) - \frac{\pi^2}{6}\right\}, \qquad (B24)$$

$$C_0(0, t, m_h^2; m_W^2, m_W^2, m_W^2) = C_0(m_h^2, 0, t; m_W^2, m_W^2, m_W^2)$$

$$= \frac{1}{t - m_h^2}\left\{ \frac{1}{2}\log^2\left(\frac{\sqrt{4 - t_W} + \sqrt{-t_W}}{\sqrt{4 - t_W} - \sqrt{-t_W}}\right) + 2\left[\sin^{-1}\sqrt{\frac{h_W}{4}}\right]^2\right\}, \qquad (B25)$$

$$C_0(0, s, m_h^2; m_Z^2, 0, m_Z^2) = \frac{-1}{s - m_h^2}\left\{ \text{Li}_2\left(\frac{1}{(s_Z - h_Z)x_{Z_+} + 1}\right) + \text{Li}_2\left(\frac{1}{(s_Z - h_Z)x_{Z_-} + 1}\right)\right.$$

$$- \text{Li}_2\left(\frac{s_Z - h_Z + 1}{(s_Z - h_Z)x_{Z_+} + 1}\right) - \text{Li}_2\left(\frac{s_Z - h_Z + 1}{(s_Z - h_Z)x_{Z_-} + 1}\right)$$

$$- \text{Li}_2(h_Z - s_Z) + \text{Li}_2\left(\frac{(s_Z - 1)(s_Z - h_Z)}{s_Z^2 - h_Z s_Z + h_Z}\right) - \text{Li}_2\left(\frac{h_Z - s_Z}{s_Z^2 - h_Z s_Z + h_Z}\right)$$

$$+ \log(s_Z - h_Z + 1)\log\left(\frac{s_Z^2 - s_Z h_Z + h_Z}{(s_Z - h_Z)^2}\right) + \log(s_Z - 1)\log\left(\frac{s_Z}{s_Z^2 - s_Z h_Z + h_Z}\right)$$

$$\left. + i\pi\log\left(\frac{s_Z^2 - s_Z h_Z + h_Z}{s_Z}\right)\right\}, \qquad (B26)$$

$$C_0(0, u, m_h^2; m_Z^2, 0, m_Z^2) = \frac{-1}{u - m_h^2}\left\{ \text{Li}_2\left(\frac{1}{1 + (u_Z - h_Z)x_{Z_+}}\right) + \text{Li}_2\left(\frac{1}{1 + (u_Z - h_Z)x_{Z_-}}\right)\right.$$

$$- \text{Li}_2\left(\frac{u_Z - h_Z + 1}{1 + (u_Z - h_Z)x_{Z_+}}\right) - \text{Li}_2\left(\frac{u_Z - h_Z + 1}{1 + (u_Z - h_Z)x_{Z_-}}\right)$$

$$\left. + \text{Li}_2(u_Z - h_Z + 1) - \text{Li}_2\left(\frac{u_Z}{u_Z^2 - h_Z u_Z + h_Z}\right) + \text{Li}_2\left(\frac{u_Z(u_Z - h_Z + 1)}{u_Z^2 - h_Z u_Z + h_Z}\right) - \frac{\pi^2}{6}\right\}. \qquad (B27)$$

The following two three-point integrals have collinear divergences which are regularized by dimensional regularization. Both integrals are in the form of $C_0(0, 0, p^2; m^2, 0, 0)$, which corresponds to "Triangle 3," $I_3^D(0, p_2^2, p_3^2; 0, 0, m^2)$ with $p_3^2 = 0$, of Ref. [23]. Its expression is given in Eq. (4.8) of Ref. [23]. For $C_0(0, 0, s; m_Z^2, 0, 0)$, we need an analytic continuation of the variable s from $s < 0$ to $s > m_Z^2$.

$$C_0(0,0,s;m_Z^2,0,0) = -\left(\frac{4\pi\mu^2}{m_Z^2}\right)^\epsilon \frac{1}{s} \left\{ \frac{1}{\epsilon}[\log(s_Z-1) - i\pi] - \frac{1}{2}[\log(s_Z-1) - i\pi]^2 \right.$$
$$\left. - \text{Li}_2\left(\frac{s_Z-1}{s_Z}\right) - \frac{1}{2}\log^2\left(\frac{s_Z}{s_Z-1}\right) + \frac{\pi^2}{3} - i\pi\log\left(\frac{s_Z}{s_Z-1}\right) \right\}, \tag{B28}$$

$$C_0(0,0,u;m_Z^2,0,0) = -\left(\frac{4\pi\mu^2}{m_Z^2}\right)^\epsilon \frac{1}{u} \left\{ \frac{1}{\epsilon}\log(1-u_Z) + \text{Li}_2\left(\frac{-u_Z}{1-u_Z}\right) - \frac{1}{2}\log^2(1-u_Z) \right\}. \tag{B29}$$

3. Four-point integrals

The four-point integrals $D_0(0,0,0,m_h^2;t,u;m_W^2,0,m_W^2,m_W^2)$ and $D_0(0,0,0,m_h^2;s,t;m_W^2,m_W^2,0,m_W^2)$ appear in Eqs. (2.15) and (2.16). Due to the relation

$$D_0(0,0,0,m_h^2;t,u;m_W^2,0,m_W^2,m_W^2) = D_0(m_h^2,0,0,0;u,t;m_W^2,m_W^2,0,m_W^2),$$

these two integrals correspond to the one given in Eq. (37) of Ref. [24]. After the analytic continuation procedure for both dilogarithms and logarithms [23], we obtain

$$D_0(0,0,0,m_h^2;t,u;m_W^2,0,m_W^2,m_W^2) = D_0(m_h^2,0,0,0;u,t;m_W^2,m_W^2,0,m_W^2)$$
$$= \frac{1}{m_W^4} \frac{1}{\sqrt{t_W^2(u_W-1)^2 - 2t_W(2u_W^2 - u_W h_W + h_W) + h_W^2}}$$
$$\times \left\{ \text{Li}_2\left(-\frac{s_1}{rx_1}\right) - \text{Li}_2\left(-\frac{s_1}{rx_2}\right) + \text{Li}_2\left(-\frac{s_2}{rx_1}\right) - \text{Li}_2\left(-\frac{s_2}{rx_2}\right) + \text{Li}_2\left(\frac{rx_1}{u_W-1}\right) \right.$$
$$+ \text{Li}_2\left(\frac{u_W-1}{rx_2}\right) - \text{Li}_2\left(\frac{x_1}{u_W-1}\right) - \text{Li}_2\left(\frac{u_W-1}{x_2}\right) - 2\text{Li}_2\left(-\frac{1}{x_1}\right) + 2\text{Li}_2\left(-\frac{1}{x_2}\right)$$
$$+ \log(s_2)\log\left(-\frac{rx_2+s_1}{rx_1+s_1}\right) + \log(s_1)\log\left(-\frac{rx_2+s_2}{rx_1+s_2}\right)$$
$$+ \log(r)\log\left(\frac{x_1^2(x_2+1)^2(u_W-x_1-1)}{x_2(x_1+1)^2(u_W-x_2-1)}\right)$$
$$\left. + \log(1-u_W)\log\left(\frac{(-u_W+x_1+1)(rx_2-u_W+1)}{r(-u_W+x_2+1)(rx_1-u_W+1)}\right) + \frac{\log^2(r)}{2} \right\}, \tag{B30}$$

where

$$r = 1 - \frac{1}{2}t_W\left(1 + \sqrt{1 - \frac{4}{t_W}}\right), \qquad s_1 = -\frac{x_{W+}}{x_{W-}}, \qquad s_2 = -\frac{x_{W-}}{x_{W+}}, \tag{B31}$$

$$x_1 = \frac{1}{4}\left(\sqrt{1 - \frac{4}{t_W}} - 1\right)\left\{ h_W + (1-u_W)t_W\sqrt{1 - \frac{4}{t_W}} \right.$$
$$\left. + \sqrt{t_W^2(1-u_W)^2 - 2t_W(2u_W^2 - u_W h_W + h_W) + h_W^2} \right\}, \tag{B32}$$

$$x_2 = \frac{1}{4}\left(\sqrt{1 - \frac{4}{t_W}} - 1\right)\left\{ h_W + (1-u_W)t_W\sqrt{1 - \frac{4}{t_W}} \right.$$
$$\left. - \sqrt{t_W^2(1-u_W)^2 - 2t_W(2u_W^2 - u_W h_W + h_W) + h_W^2} \right\}, \tag{B33}$$

$$D_0(0,0,0,m_h^2;s,t;m_W^2,m_W^2,0,m_W^2) = \frac{1}{m_W^4}\frac{1}{\sqrt{t_W^2(s_W-1)^2 - 2t_W(2s_W^2 - s_Wh_W + h_W) + h_W^2}}$$

$$\times \left\{ -\text{Li}_2\left(\frac{s_W-1}{ry_1}\right) - \text{Li}_2\left(\frac{ry_2}{s_W-1}\right) + 2\text{Li}_2\left(-\frac{1}{ry_1}\right) - 2\text{Li}_2\left(-\frac{1}{ry_2}\right) - \text{Li}_2\left(-\frac{s_1}{y_1}\right) + \text{Li}_2\left(-\frac{s_1}{y_2}\right) \right.$$

$$- \text{Li}_2\left(-\frac{s_2}{y_1}\right) + \text{Li}_2\left(-\frac{s_2}{y_2}\right) + \text{Li}_2\left(\frac{s_W-1}{y_1}\right) + \text{Li}_2\left(\frac{y_2}{s_W-1}\right)$$

$$+ \log(r)\log\left(\frac{y_1(ry_2+1)^2(ry_1-s_W+1)}{y_2^2(ry_1+1)^2(ry_2-s_W+1)}\right) + \log(s_1)\log\left(\frac{(s_1+y_2)(s_2+y_1)}{(s_1+y_1)(s_2+y_2)}\right)$$

$$+ \log(s_W-1)\log\left(\frac{r(-s_W+y_1+1)(ry_2-s_W+1)}{(-s_W+y_2+1)(ry_1-s_W+1)}\right) - \frac{1}{2}\log^2(r)$$

$$\left. + i\pi\log\left(\frac{(-s_W+y_2+1)(ry_1-s_W+1)}{(-s_W+y_1+1)(ry_2-s_W+1)}\right) \right\}, \tag{B34}$$

where r, s_1 and s_2 are given in Eq. (B31) and

$$y_1 = \frac{1}{4}\left(\sqrt{1-\frac{4}{t_W}}-1\right)\left\{ -h_W - (s_W-1)t_W\sqrt{1-\frac{4}{t_W}} \right.$$

$$\left. + \sqrt{t_W^2(s_W-1)^2 - 2t_W(2s_W^2 - h_Ws_W + h_W) + h_W^2} \right\}, \tag{B35}$$

$$y_2 = \frac{1}{4}\left(\sqrt{1-\frac{4}{t_W}}-1\right)\left\{ -h_W - (s_W-1)t_W\sqrt{1-\frac{4}{t_W}} \right.$$

$$\left. - \sqrt{t_W^2(s_W-1)^2 - 2t_W(2s_W^2 - h_Ws_W + h_W) + h_W^2} \right\}. \tag{B36}$$

The four-point integral $D_0(0,0,0,m_h^2;s,u;m_Z^2,0,0,m_Z^2)$, which appears in Eqs. (2.19) and (2.20), corresponds to the one given in Eq. (4.37) of Ref. [23] and also in Eq. (4.13) of Ref. [25]. It has a collinear singularity. After the analytic continuation procedure for both dilogarithms and logarithms [23], we obtain

$$D_0(0,0,0,m_h^2;s,u;m_Z^2,0,0,m_Z^2) = D_0(0,0,m_h^2,0;s,u;0,0,m_Z^2,m_Z^2)$$

$$= \frac{1}{su - m_Z^2(s+u)}\left\{ \left(\frac{4\pi\mu^2}{m_Z^2}\right)^\epsilon e^{-\epsilon\gamma_E} \times \frac{1}{\epsilon}\left[-[\log(s_Z-1) - i\pi] - \log(1-u_Z) \right] \right.$$

$$+ 2\text{Li}_2\left(\frac{s_Z-1}{s_Z}\right) - 2\text{Li}_2\left(-\frac{u_Z}{1-u_Z}\right) - 2\text{Li}_2\left(\frac{1}{(1-s_Z)(1-u_Z)}\right)$$

$$+ \text{Li}_2\left(-\frac{x_{Z_+}}{x_{Z_-}(1-s_Z)}\right) + \text{Li}_2\left(-\frac{x_{Z_-}}{x_{Z_+}(1-s_Z)}\right) + \text{Li}_2\left(1 + \frac{x_{Z_+}(1-u_Z)}{x_{Z_-}}\right) + \text{Li}_2\left(1 + \frac{x_{Z_-}(1-u_Z)}{x_{Z_+}}\right)$$

$$+ \log^2\left(\frac{s_Z}{s_Z-1}\right) + 2\log((s_Z-1)(1-u_Z))\log\left(\frac{s_Z+u_Z-u_Zs_Z}{(s_Z-1)(1-u_Z)}\right) + 2\log(s_Z-1)\log(1-u_Z)$$

$$+ \log^2(1-u_Z) + \log\left(1 + \frac{x_{Z_+}}{x_{Z_-}(1-s_Z)}\right)\left\{\log\left(-\frac{x_{Z_+}}{x_{Z_-}}\right) - \log(s_Z-1)\right\}$$

$$+ \log\left(1 + \frac{x_{Z_-}}{x_{Z_+}(1-s_Z)}\right)\left\{\log\left(-\frac{x_{Z_-}}{x_{Z_+}}\right) - \log(s_Z-1)\right\} - \frac{2\pi^2}{3}$$

$$\left. + i\pi\left[2\log\left(\frac{s_Z}{s_Z+u_Z-u_Zs_Z}\right) + \log\left(1 + \frac{x_{Z_+}}{x_{Z_-}(1-s_Z)}\right) + \log\left(1 + \frac{x_{Z_-}}{x_{Z_+}(1-s_Z)}\right)\right] \right\}. \tag{B37}$$

APPENDIX C: INTERFERENCE TERMS

We write down the contributions from the interference terms of $\sum_{\text{final electron spin}} |A(P_e, P_p)|^2$,

$$\sum_{\text{spin}} [A^*_{\gamma\gamma}(P_e, P_\gamma) A_{Z\gamma}(P_e, P_\gamma) + A_{\gamma\gamma}(P_e, P_\gamma) A^*_{Z\gamma}(P_e, P_\gamma)]$$

$$= \left(\frac{e^2 g^2}{16\pi^2}\right)^2 \left(\frac{-2}{t - m_Z^2}\right) F_{\gamma\gamma} F_{Z\gamma} \left\{ (f_{Ze} + P_e) \frac{s^2 + u^2}{(s + u)^2} + P_\gamma (f_{Ze} P_e + 1)\left(1 - \frac{2u}{s + u}\right) \right\}, \tag{C1}$$

$$\sum_{\text{spin}} [A^*_{\gamma\gamma}(P_e, P_\gamma) A_{W\nu_e}(P_e, P_\gamma) + A_{\gamma\gamma}(P_e, P_\gamma) A^*_{W\nu_e}(P_e, P_\gamma)]$$

$$= \left(\frac{e^2 g^2}{16\pi^2}\right)^2 \frac{-m_W}{2} F_{\gamma\gamma} (1 - P_e) \frac{1}{s + u}$$

$$\times \{ -s \,\mathrm{Re}[S^{W\nu_e}_{(k_1)}(s, t, m_h^2, m_W^2)] + u \,\mathrm{Re}[S^{W\nu_e}_{(k_1')}(s, t, m_h^2, m_W^2)]$$

$$+ P_\gamma(s \,\mathrm{Re}[S^{W\nu_e}_{(k_1)}(s, t, m_h^2, m_W^2)] + u \,\mathrm{Re}[S^{W\nu_e}_{(k_1')}(s, t, m_h^2, m_W^2)]) \}, \tag{C2}$$

$$\sum_{\text{spin}} [A^*_{\gamma\gamma}(P_e, P_\gamma) A_{Ze}(P_e, P_\gamma) + A_{\gamma\gamma}(P_e, P_\gamma) A^*_{Ze}(P_e, P_\gamma)]$$

$$= \left(\frac{e^2 g^2}{16\pi^2}\right)^2 \left(-\frac{m_Z}{8\cos^3\theta_W}\right) \frac{1}{s + u} F_{\gamma\gamma}$$

$$\times \{ (f_{Ze}^2 + 2P_e f_{Ze} + 1)\{ s \,\mathrm{Re}[S^{Ze}_{(k_1)}(s, t, m_h^2, m_Z^2)] - u \,\mathrm{Re}[S^{Ze}_{(k_1')}(s, t, m_h^2, m_Z^2)] \}$$

$$+ P_\gamma(P_e f_{Ze}^2 + 2f_{Ze} + P_e)\{ s \,\mathrm{Re}[S^{Ze}_{(k_1)}(s, t, m_h^2, m_Z^2)] + u \,\mathrm{Re}[S^{Ze}_{(k_1')}(s, t, m_h^2, m_Z^2)] \} \}, \tag{C3}$$

$$\sum_{\text{spin}} [A^*_{Z\gamma}(P_e, P_\gamma) A_{W\nu_e}(P_e, P_\gamma) + A_{Z\gamma}(P_e, P_\gamma) A^*_{W\nu_e}(P_e, P_\gamma)]$$

$$= \left(\frac{e g^3}{16\pi^2}\right)^2 \frac{m_W}{2} \left(\frac{-t}{t - m_Z^2}\right) (1 - P_e)(f_{Ze} - 1) F_{Z\gamma} \frac{1}{s + u}$$

$$\times \{ -s \,\mathrm{Re}[S^{W\nu_e}_{(k_1)}(s, t, m_h^2, m_W^2)] + u \,\mathrm{Re}[S^{W\nu_e}_{(k_1')}(s, t, m_h^2, m_W^2)]$$

$$+ P_\gamma\{ s \,\mathrm{Re}[S^{W\nu_e}_{(k_1)}(s, t, m_h^2, m_W^2)] + u \,\mathrm{Re}[S^{W\nu_e}_{(k_1')}(s, t, m_h^2, m_W^2)] \} \}, \tag{C4}$$

$$\sum_{\text{spin}} [A^*_{Z\gamma}(P_e, P_\gamma) A_{Ze}(P_e, P_\gamma) + A_{Z\gamma}(P_e, P_\gamma) A^*_{Ze}(P_e, P_\gamma)]$$

$$= \left(\frac{e g^3}{16\pi^2}\right)^2 \left(-\frac{m_Z}{16\cos^3\theta_W}\right) \left(\frac{1}{t - m_Z^2}\right) F_{Z\gamma} \frac{2t}{s + u}$$

$$\times \{ (f_{Ze}^3 + 3f_{Ze}^2 P_e + 3f_{Ze} + P_e)\{ s \,\mathrm{Re}[S^{Ze}_{(k_1)}(s, t, m_h^2, m_Z^2)] - u \,\mathrm{Re}[S^{Ze}_{(k_1')}(s, t, m_h^2, m_Z^2)] \}$$

$$+ P_\gamma(f_{Ze}^3 P_e + 3f_{Ze}^2 + 3f_{Ze} P_e + 1)\{ s \,\mathrm{Re}[S^{Ze}_{(k_1)}(s, t, m_h^2, m_Z^2)] + u \,\mathrm{Re}[S^{Ze}_{(k_1')}(s, t, m_h^2, m_Z^2)] \} \}, \tag{C5}$$

$$\sum_{\text{spin}} [A^*_{W\nu_e}(P_e, P_\gamma) A_{Ze}(P_e, P_\gamma) + A_{W\nu_e}(P_e, P_\gamma) A^*_{Ze}(P_e, P_\gamma)]$$

$$= \left(\frac{e g^3}{16\pi^2}\right)^2 \frac{m_W}{4} \left(-\frac{m_Z}{16\cos^3\theta_W}\right) (1 - P_e)(f_{Ze} - 1)^2 (-2t)$$

$$\times \{ \mathrm{Re}\{ [S^{W\nu_e}_{(k_1)}(s, t, m_h^2, m_W^2)][S^{Ze}_{(k_1)}(s, t, m_h^2, m_Z^2)]^* + [S^{W\nu_e}_{(k_1')}(s, t, m_h^2, m_W^2)][S^{Ze}_{(k_1')}(s, t, m_h^2, m_Z^2)]^* \}$$

$$+ P_\gamma \mathrm{Re}\{ -[S^{W\nu_e}_{(k_1)}(s, t, m_h^2, m_W^2)][S^{Ze}_{(k_1)}(s, t, m_h^2, m_Z^2)]^*$$

$$+ [S^{W\nu_e}_{(k_1')}(s, t, m_h^2, m_W^2)][S^{Ze}_{(k_1')}(s, t, m_h^2, m_Z^2)]^* \} \}. \tag{C6}$$

With the fact that $S^{W\nu_e}_{(k'_1)}$ and $S^{Ze}_{(k'_1)}$ vanish as $u \to 0$, it is easy to see that the contributions from the interference terms reduce to zero as $u \to 0$ when $P_e P_\gamma = -1$.

[1] ATLAS Collaboration, Phys. Lett. B **716**, 1 (2012); CMS Collaboration, Phys. Lett. B **716**, 30 (2012).

[2] ATLAS Collaboration, Phys. Lett. B **726**, 88 (2013); Phys. Lett. B **726**, 120 (2013); CMS Collaboration, Phys. Rev. Lett. **110**, 081803 (2013).

[3] http://www.linearcollider.org.

[4] A. De Roeck, arXiv:hep-ph/0311138.

[5] V. I. Telnov, Nucl. Instrum. Methods Phys. Res., Sect. A **455**, 63 (2000); B. Badelek et al., Int. J. Mod. Phys. A **19**, 5097 (2004); M. M. Velasco et al., eConf C010630, E3005 (2001).

[6] M. Melles, W. J. Stirling, and V. A. Khoze, Phys. Rev. D **61**, 054015 (2000); M. Melles, Nucl. Phys. B, Proc. Suppl. **82**, 379 (2000); G. Jikia and S. Soldner-Rembold, Nucl. Phys. B, Proc. Suppl. **82**, 373 (2000); M. M. Mühlleitner, M. Krämer, M. Spira, and P. M. Zerwas, Phys. Lett. B **508**, 311 (2001); M. M. Mühlleitner, Acta Phys. Pol. B **37**, 1127 (2006); D. M. Asner, J. B. Gronberg, and J. F. Gunion, Phys. Rev. D **67**, 035009 (2003); S. J. Brodsky, Int. J. Mod. Phys. A **20**, 7306 (2005); P. Niezurawski, eConf C050318, 0503 (2005).

[7] S. A. Bogacz et al., arXiv:1208.2827.

[8] I. F. Ginzburg and M. Krawczyk, arXiv:1310.5881; I. F. Ginzburg and M. V. Vychugin, Phys. At. Nucl. **67**, 281 (2004).

[9] N. Watanabe, Y. Kuriharam, K. Sasaki, and T. Uematsu, Phys. Lett. B **728**, 202 (2014); Proc. Sci., RADCOR (2013) 050; Proc. Sci., RADCOR (2013) 053; Proc. Sci., QFTHEP (2013) 040.

[10] E. Gabrielli, V. A. Ilyin, and B. Mele, Phys. Rev. D **56**, 5945 (1997); **60**, 113005 (1999).

[11] O. J. P. Éboli, M. C. Gonzales-Garcia, and S. F. Novaes, Phys. Rev. D **49**, 91 (1994).

[12] http://www.feyncalc.org.

[13] G. Passarino and M. Veltman, Nucl. Phys. **B160**, 151 (1979); G.'t Hooft and M. J. G. Veltman, Nucl. Phys. **B153**, 365 (1979); G. J. van Oldenborgh and J. A. M. Vermaseren, Z. Phys. C **46**, 425 (1990).

[14] J. Ellis, M. K. Gaillard, and D. V. Nanopoulos, Nucl. Phys. **B106**, 292 (1976); B. L. Ioffe and V. A. Khoze, Sov. J. Part. Nucl. **9**, 50 (1978); M. A. Shifman, A. I. Vainshtein, M. B. Voloshin, and V. I. Zakharov, Sov. J. Nucl. Phys. **30**, 711 (1979); M. A. Shifman, A. I. Vainshtein, M. B. Voloshin, and V. I. Zakharov, Phys. Rev. D **85**, 013015 (2012); T. G. Rizzo, Phys. Rev. D **22**, 178 (1980); M. B. Gavela, G. Girardi, C. Malleville, and P. Sorba, Nucl. Phys. **B193**, 257 (1981); W. J. Marciano, C. Zhang, and S. Willenbrock, Phys. Rev. D **85**, 013002 (2012).

[15] J. F. Gunion, H. E. Haber, G. Kane, and S. Dawason, *The Higgs Hunter's Guide* (Addison-Wesley, Reading, MA, 1990).

[16] I. F. Ginzburg, G. L. Kotkin, V. G. Serbo, and V. I. Telnov, Nucl. Instrum. Methods Phys. Res., Sect. A **205**, 47 (1983); I. F. Ginzburg, G. L. Kotkin, S. L. Panfil, V. G. Serbo, and V. I. Telnov, Nucl. Instrum. Methods Phys. Res., Sect. A **219**, 5 (1984); V. I. Telnov, Nucl. Instrum. Methods Phys. Res., Sect. A **294**, 72 (1990); Nucl. Instrum. Methods Phys. Res., Sect. A **355**, 3 (1995).

[17] A. M. Sessler, Conference Proceedings **C950501**, 30 (1995); K. Kim and A. Sessler, SLAC Beam Line **26**, 16 (1996).

[18] F. Yuasa, Y. Kurihara and S. Kawabata, Phys. Lett. B **414**, 178 (1997); F. Yuasa et al., Prog. Theor. Phys. Suppl. **138**, 18 (2000).

[19] T. Omori et al., Phys. Rev. Lett. **67**, 3294 (1991).

[20] M. Drees and K. Grassie, Z. Phys. C **28**, 451 (1985); H. Abramowicz, K. Charchula, and A. Levy, Phys. Lett. B **269**, 458 (1991).

[21] M. Glück, E. Reya, and A. Vogt, Phys. Rev. D **46**, 1973 (1992).

[22] E. Witten, Nucl. Phys. **B120**, 189 (1977); W. A. Bardeen and A. J. Buras, Phys. Rev. D **20**, 166 (1979); K. Sasaki, Phys. Rev. D **22**, 2143 (1980); M. Stratmann and W. Vogelsang, Phys. Lett. B **386**, 370 (1996); K. Sasaki J. Soffer and T. Uematsu, Phys. Lett. B **522**, 22 (2001); N. Watanabe, Y. Kiyo, and K. Sasaki, Phys. Rev. D **88**, 034022 (2013).

[23] R. K. Ellis and G. Zanderighi, J. High Energy Phys. 02 (2008) 002.

[24] A. Denner, U. Nierste, and R. Scharf, Nucl. Phys. **B367**, 637 (1991).

[25] A. Denner and S. Dittmaier, Nucl. Phys. **B844**, 199 (2011).